

TOPICAL REVIEW • OPEN ACCESS

Intrinsic charge trapping in amorphous oxide films: status and challenges

To cite this article: Jack Strand *et al* 2018 *J. Phys.: Condens. Matter* **30** 233001

View the [article online](#) for updates and enhancements.

Related content

- [Theoretical modeling of charge trapping in crystalline and amorphous Al₂O₃](#)
Oliver A Dicks and Alexander L Shluger
- [A mechanism for Frenkel defect creation in amorphous SiO₂ facilitated by electron injection](#)
David Z Gao, Al-Moatasem El-Sayed and Alexander L Shluger
- [Modelling of electron and hole trapping in oxides](#)
A L Shluger, K P McKenna, P V Sushko et al.

Topical Review

Intrinsic charge trapping in amorphous oxide films: status and challenges

Jack Strand¹, Moloud Kaviani², David Gao¹, Al-Moatasem El-Sayed¹, Valeri V Afanas'ev³ and Alexander L Shluger^{1,2,4}

¹ Department of Physics, University College London, Gower Street, London WC1E 6BT, United Kingdom

² WPI-Advanced Institute for Materials Research, Tohoku University, Sendai 980-8577, Japan

³ Department of Physics, University of Leuven, Celestijnenlaan 200D, 3001 Leuven, Belgium

⁴ London Centre for Nanotechnology, University College London, Gower Street, London WC1E 6BT, United Kingdom

E-mail: a.shluger@ucl.ac.uk

Received 29 January 2018, revised 5 April 2018


Accepted for publication 25 April 2018

Published 15 May 2018



Abstract

We review the current understanding of intrinsic electron and hole trapping in insulating amorphous oxide films on semiconductor and metal substrates. The experimental and theoretical evidences are provided for the existence of intrinsic deep electron and hole trap states stemming from the disorder of amorphous metal oxide networks. We start from presenting the results for amorphous (a) HfO₂, chosen due to the availability of highest purity amorphous films, which is vital for studying their *intrinsic* electronic properties. Exhaustive photo-depopulation spectroscopy measurements and theoretical calculations using density functional theory shed light on the atomic nature of electronic gap states responsible for deep electron trapping observed in a-HfO₂. We review theoretical methods used for creating models of amorphous structures and electronic structure calculations of amorphous oxides and outline some of the challenges in modeling defects in amorphous materials. We then discuss theoretical models of electron polarons and bi-polarons in a-HfO₂ and demonstrate that these intrinsic states originate from low-coordinated ions and elongated metal-oxygen bonds in the amorphous oxide network. Similarly, holes can be captured at under-coordinated O sites. We then discuss electron and hole trapping in other amorphous oxides, such as a-SiO₂, a-Al₂O₃, a-TiO₂. We propose that the presence of low-coordinated ions in amorphous oxides with electron states of significant *p* and *d* character near the conduction band minimum can lead to electron trapping and that deep hole trapping should be common to all amorphous oxides. Finally, we demonstrate that bi-electron trapping in a-HfO₂ and a-SiO₂ weakens Hf(Si)-O bonds and significantly reduces barriers for forming Frenkel defects, neutral O vacancies and O²⁻ ions in these materials. These results should be useful for better understanding of electronic properties and structural evolution of thin amorphous films under carrier injection conditions.

 Original content from this work may be used under the terms of the [Creative Commons Attribution 3.0 licence](https://creativecommons.org/licenses/by/3.0/). Any further distribution of this work must maintain attribution to the author(s) and the title of the work, journal citation and DOI.

Keywords: amorphous oxides, charge trapping, Frenkel defects, ab initio calculations

(Some figures may appear in colour only in the online journal)

1. Introduction

Thin metal oxide films grown on different substrates via oxidation and deposition are ubiquitous in the environment and across a wide range of technologies. Their atomic network structures are strongly affected by interfaces and may differ significantly from those of bulk materials, resulting in a number of unusual electrical, physical and chemical characteristics recognized in earlier studies [1, 2]. Importantly, such films can grow either (poly)-crystalline or amorphous, dependent on the deposition and anneal conditions and film thickness. Amorphous metal oxide films are used in a broad variety of applications that require reduced oxide thickness alongside mechanical flexibility and reliability. This rich research field has been harvested by various communities, often addressing the same material but from different perspectives. Oxide surface science deals with the structure and chemical properties of oxidized metals [3] whereas corrosion science is interested in the kinetics and thermodynamics of metal oxidation [4]. Amorphous oxide semiconductors (AOS) are the subject of another thriving community. AOSs have undergone tremendous development during the past few years with display companies starting mass production of commercial products that integrate AOS thin film transistor (TFT) backplanes and new applications emerging, such as electron injection and transport layers in organic light-emitting diodes [5]. The design and characterization of AOS for transparent conductors and TFTs has been reviewed in [6–8]. These studies focus mainly on the effects of disorder on the carrier mobility in the oxide [6, 8]. Non-crystalline oxides used in many other areas, most prominently oxide glasses in optics, opto-electronics and photonics, are also well investigated. One of the most important glass formers—silica (SiO_2) produced by oxidizing Si substrates—has been used as the gate dielectric in micro-electronics for the last 50 years. However, scaling of metal–oxide–semiconductor (MOS) devices led to the dramatic reduction of thickness of gate SiO_2 layers eventually leading to a materials revolution [9–11] with many other oxide films now being used in transistors, memory cells, spintronic devices and displays along side with high-mobility semiconductors [12], carbon nanotubes, graphene and 2D materials [11, 13].

A typical system considered in this review is shown in figure 1, which exhibits high-resolution transmission electron microscopy (HRTEM) images of a 2 nm amorphous HfO_2 film grown on the Si(1 0 0) substrate. A thin $\alpha\text{-SiO}_2$ film grows between Si and HfO_2 due to oxidation of the Si substrate. The film morphology changes as a result of anneal and the HfO_2 film becomes partially crystallized, as can be seen in figure 1(d). The primary function of these oxide films is to serve as gate *dielectrics* but strain and disorder in ultra-thin interface layers causes them to behave differently from their bulk crystalline counterparts. The early concerns that defective

grain boundary regions in poly-crystalline films may enhance unwanted electronic conduction through films [15, 16] prompted wide applications of amorphous dielectrics. When devices are under operating conditions, these films are subjected to electrical stress and charge carrier injection. Charge accumulation inside films and electrical current through them may lead to changes in their structure and properties. In the context of MOS devices, the trapping-induced charge buildup in the gate dielectric leads to transistor threshold voltage shift and degradation of carrier mobility in semiconductor channel [17], which makes the density of traps critical for device reliability assessment. On the other hand, in some other applications the presence of charge is desirable. For example, in silicon solar cells $\alpha\text{-Al}_2\text{O}_3$ layers with a significant density of fixed negative charge are used to achieve electrostatic passivation [18–20] by introducing substantial band bending at the silicon side of the Si/ $\alpha\text{-Al}_2\text{O}_3$ interface. This leads to a reduction of the surface recombination velocity thus improving the solar cell efficiency.

Amorphous metal oxide dielectrics that are attracting particular interest due to their wide applications [11, 21–24], such as ZrO_2 , HfO_2 , Al_2O_3 , MgO , ZnO , and TiO_2 , are not glass-formers. Unlike SiO_2 , which has been traditionally employed in opto- and micro-electronic technologies, thin amorphous films of these oxides deposited on substrates are much less stable and prone to structural transformations in the course of technological processing and operation. However, little is known about how their structure affects the ability of the oxide film to remain electrically neutral under bias application and carrier injection conditions, which is the key property of the insulating material required to enable the efficient electric field control in a transistor devices by applying a bias voltage to the gate electrode. Our status report will mainly focus on the behavior of electrons and holes in amorphous dielectrics used in nano-electronic devices with particular attention to the charge trapping in the insulating film. However, it benefits from and touches upon many common issues pertaining to the structure and properties of thin amorphous oxide films studied for other purposes.

Native defects, such as oxygen vacancies, and impurities, e.g. hydrogen and metal ions, are known to serve as electron and hole trapping sites in crystalline oxide films. Polarons have also been predicted to exist in some crystalline oxides. Much less is known about amorphous films which have different atomic structure and band gaps and, therefore, can accommodate charge differently. In particular, the reduced density and increased disorder in amorphous oxide networks both lead to the presence of a significant fraction of ions having reduced coordination with respect to bulk crystalline materials [25–29]. In this respect they are analogous to the much better studied nano-crystalline form of these oxides which can provide useful clues regarding expected behavior of ultra-thin

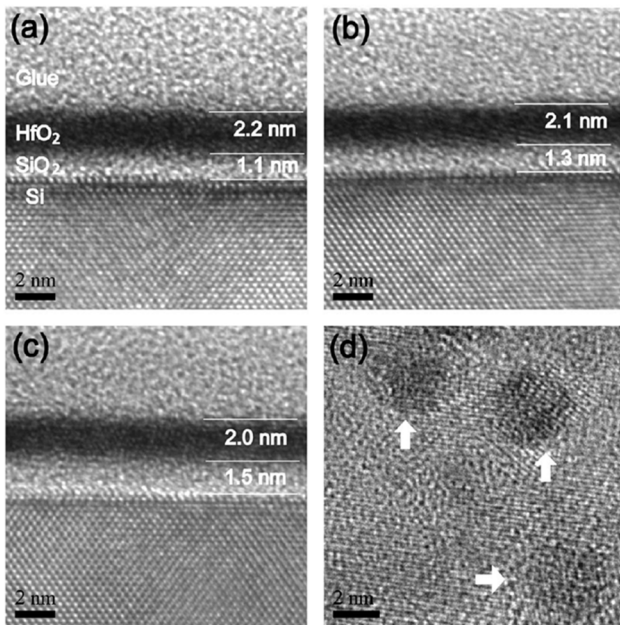


Figure 1. HRTEM images of Si/SiO₂/HfO₂ stack. (a)–(c) Cross-sectional images of 2 nm HfO₂ on Si(100) substrate annealed at 600 °C (a), 800 °C, (b) and 1000 °C (c). Thickness of the interfacial SiO₂ layer increases, while that of HfO₂ layer decreases with annealing temperature. (d) Image in plan view showing nanocrystals of orthorhombic HfO₂ from the same sample as (c). Reproduced from [14], with the permission of AIP Publishing.

amorphous films. For example, no electron or hole trapping is observed in the bulk of non-defective crystalline MgO [30]. However, both electrons and holes can be captured at low-coordinated corner and kink sites at surfaces of MgO nano-crystallites due to favorable electrostatic potential [31]. Electrons and holes form shallow polaron states in the bulk of crystalline ZrO₂, HfO₂ [32, 33] and ZnO [34], but low-coordinated sites at surfaces of these materials provide much deeper trapping sites [35, 36]. Can disorder or lower coordination of ions in the amorphous phase of such oxides also lead to intrinsic electron or hole trapping in deep states? The results of recent experimental and theoretical studies of amorphous a-HfO₂ support this hypothesis [37, 38]. However, convincingly *proving* the intrinsic nature of electron traps in nm-thick amorphous films of the type shown in figure 1 is challenging and requires synergy between theory and experiment.

We will review the experimental and theoretical evidence towards the existence of *intrinsic* deep electron and hole trap states caused by disorder in amorphous oxide films. Most of the evidence comes from theoretical calculations, which play an increasingly important role in predicting properties of thin amorphous oxide films. Experimental studies are often hampered by the presence of impurities and native defects, such as oxygen vacancies. High purity a-HfO₂ layers, which can now be grown for MOS applications, allow us to get insight into their *intrinsic* properties unaffected by contaminants. With the gradual downscaling of the MOS devices, the oxide dielectric has now reached nanometer dimensions introducing the stochastically distributed characteristics. These characteristics

are studied mainly using very sensitive electrical measurements, such as charge pumping, extended measure-stress-measure and the time-dependent defect spectroscopy techniques discussed in detail in [17]. The recently developed exhaustive photo-depopulation spectroscopy (EPDS) [39–41] allows one to probe the energy distribution of electronic states in the oxide bandgap associated with negative charging of oxide films. Unlike the defect spectroscopy techniques based on time-dependent degradation measurements (see e.g. [42]), this technique allows direct comparison between the calculated defect properties and photo-depopulation energy spectra of defect states. Therefore we focus on discussing EPDS measurements to provide insight into the methods used to study electron trapping in amorphous films. Combined with this we provide discussion of density functional theory (DFT) based theoretical calculations to study the atomic nature of electronic gap states responsible for charge trapping.

As a first example we use a-HfO₂ films [37] where it has been demonstrated that electron trapping is insensitive to the particular chemistry of oxide synthesis, i.e. is intrinsic and originates from lower coordination of ions and elongation of bonds. Theoretical calculations predict that holes can also trap at under-coordinated O sites in a-HfO₂ [38]. We discuss how electron and hole trapping can be relevant to other amorphous oxides, such as a-SiO₂, a-Al₂O₃, a-TiO₂ as well as indium gallium zinc oxide and propose that the presence of low-coordinated ions in other amorphous oxides with significant *p* and *d* character of electron states near the conduction band minimum (CBM) can lead to electron trapping and that deep hole trapping should be common to all amorphous oxides. Finally, we demonstrate that bi-electron trapping in a-HfO₂ and a-SiO₂ weakens Hf(Si)–O bonds and significantly reduces barriers for the formation of Frenkel defects, neutral oxygen vacancies and O²⁻ ions in these materials.

We note that the conventional solid state description of the violation of electro-neutrality is associated with charge carrier trapping at ‘defective’ sites of the crystalline or amorphous network, such as vacancies, interstitials or dangling bonds etc. In contrast, the results presented below suggest that charging of amorphous oxides may occur by electron trapping on ‘intrinsic’, i.e. not related to any damage, network fragments. This new paradigm in this field significantly changes the view on the physics of charging phenomena. This paradigm is essential for better understanding of peculiar electronic and electrical properties of amorphous films used in microelectronics, thin-film transistors and opto-electronics applications. Carrier injection and conduction are also vital for photo-catalysis, corrosion and other electrochemical systems and devices where electron-hole pairs are created by light or by carrier injection as a result of bias application. We hope that the results discussed below will be helpful for our understanding the electronic properties and structural evolution of amorphous dielectric films under carrier injection conditions. This situation is ubiquitous in fundamental studies and technologies, but challenging to investigate using physical methods. The approach demonstrated in our manuscript will advance the state-of-the-art in this field.

2. Experimental evidence of negative and positive charging of oxide films

2.1. Charge trapping in amorphous oxides

Thin films of oxide insulators on semiconductor substrates, e.g. silicon, provide the best opportunity to experimentally study electron and hole localization in amorphous matrices because charge carrier trapping leads to a build-up of fixed charges. Their sign and density can be directly monitored using non-destructive semiconductor field-effect methods [43]. In the case of conventional amorphous SiO₂ films synthesized by thermal oxidation of silicon, hole trapping occurs by far more efficiently than electron trapping. This can lead to the commonly observed positive oxide charging upon exposure to ionizing radiation [44]. Interestingly, both hole and electron trapping in thermal SiO₂ are dominated by hydrogen-containing network fragments, O₃Si–H [45] and SiO–H [46], respectively. Interstitial water molecules have also been suggested as potential electron traps [46] which would further underline dominant role of impurity-related processes in SiO₂ charging. The intrinsic electron trapping mechanism by stretched bonds and distorted SiO₄ tetrahedra in a-SiO₂ has been invoked only recently [47]. The latter is shown to account well for the experimentally observed energies of deep electron states in the a-SiO₂ gap near interfaces with Si and SiC.

In contrast to a-SiO₂, a dominance of electron trapping is commonly observed in broad variety of high-permittivity metal oxide insulators, which suggests a different charging physics [48–50]. It is striking to observe that in several insulating metal oxides, such as Al₂O₃ [39, 41, 51], Y₂O₃ [40, 51], HfO₂ [37, 39], HfAlO_x [37], GdAlO_x and LaAlO_x [51], deep electron traps exhibit similar energy distributions: a ≈1 eV wide band of electron energy levels is typically found in the energy range 2–3 eV below the conduction band minimum irrespective of the metal cation type or the oxide synthesis chemistry. The latter points towards the common, probably intrinsic in its origin, mechanism of electron localization in amorphous metal oxide insulators. Yet, the atomic structure of these trapping sites remains unknown.

Generally, hole trapping in amorphous metal oxides appears to be much less pronounced than in SiO₂ and predominantly occurs close to the SiO₂/high-*k* interface. The latter suggests that in stacked insulators the SiO₂ interlayer remains the preferred hole trapping region. This is further supported by the observation of large capture cross sections of hole trapping and their subsequent annihilation by injected electrons [52]. Nevertheless, when attempting to eliminate the influence of the SiO₂ interlayer, reliability experiments indicate surprising correlation between electron trapping and hole trapping related oxide charging phenomena [48, 53, 54]: Positive and negative charging of transistors with HfO₂ insulators does change the lifetime very similarly as the thickness of the a-SiO₂ interlayer between the silicon transistor channel and the HfO₂ gate insulator is varied using thermal processing [48]. Taking into account that these HfO₂ layers are only about 2 nm thick and remain mostly amorphous despite applied annealing treatments (see figure 1), correlated electron and

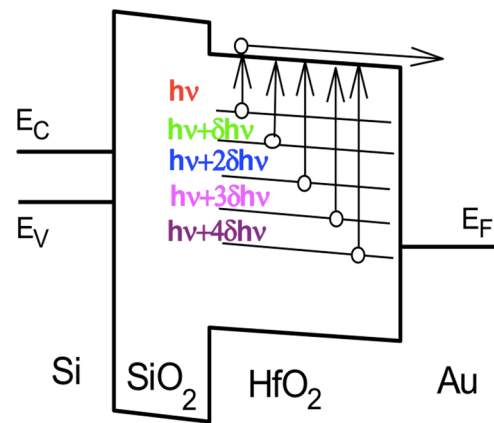


Figure 2. Schematics of electron excitations during EPDS experiments carried out on a Si/SiO₂/HfO₂/Au capacitor using incremental photon energies. A positive bias (usually +1 to +2 V) is applied to the metal gate to collect the de-trapped electrons.

hole trapping points towards the common physics of localization of charge carriers of opposite sign.

Below we discuss the experimentally measured energy distribution of trap levels in a-HfO₂. Due to the mentioned similarity, these results are representative of trap energy distributions in other amorphous metal oxides. HfO₂ and HfSi_xO_y are the primary contenders to replace SiO₂ in a variety of nano-electronic devices, ranging from deep-scaled transistors to dynamic random-access memory [11, 24], and non-volatile memory cells [55, 56]. In combination with metal gate electrodes, they have already been used in the first generation of such devices [48]. Substantial industrial investment has enabled the development of techniques that are capable of producing HfO₂ films of the utmost purity. This currently makes this material the best possible choice for studying the *intrinsic* electron and hole trapping in non-glass forming oxides.

2.2. Determination of energy distribution of trap levels in a-HfO₂

The phenomenon of photo-ionization (or photo-depopulation) of defect states with energy levels in the bandgap of an insulator is long known. However, the conventional approach consisting of the observation of this effect by using measurements of the photo-current provides only limited information because the current is determined by the rate of the optically-excited charge carrier transitions from the gap state to the state above the mobility edge. Mathematically this emission rate represents the product of the incident photon flux and of convolution of the energy-dependent distribution of trap levels and the photo-ionization cross-section. Consequently, one only can identify the energy onset of the photo-ionization process but neither the density nor energy distribution of traps can be recovered from the photo-depopulation current spectral distributions.

To resolve this problem, in the exhaustive photo-depopulation spectroscopy method one employs measurements of the insulator charge rather than current. Furthermore, EPDS allows the photo-depopulation to exhaust all charge carriers available for optical excitation at a given photon energy $h\nu$.

Starting from a low photon energy $h\nu$ and then increasing it by a small energy step $\delta h\nu$, the saturation of the de-trapping kinetics within each photon energy interval $h\nu$; $h\nu + \delta h\nu$ means that there are virtually no electrons left available for optical transitions to the conduction band in this energy window. Then, the amount of charge de-trapped during the next step will exactly correspond to the density of occupied electron states with energy levels in that energy interval $\delta h\nu$ and can be used to directly calculate the spectral charge distribution (SCD) by normalizing the emitted carrier density to the energy interval $\delta h\nu$. By performing the EPDS at incremental photon energies $h\nu$ as illustrated in figure 2, one can find the distribution of the electron states across the insulator bandgap.

The experimentally studied samples were prepared by atomic layer deposition (ALD) of HfO_2 on (100)Si wafers by production-grade ALD process using HfCl_4 and H_2O precursors at 300 °C. Some samples were subsequently annealed for 15 min in N_2 (1 atm) at 1000 °C. MOS capacitors were completed by thermo-resistive evaporation of semi-transparent electrodes (13 nm Au) of 1 mm² area on the oxide stack which excludes exposure of the insulating layers to ionizing radiation. Energy distribution of trap levels in the HfO_2 bandgap was determined by using EPDS method where the insulator charge variations were monitored using 200 kHz capacitance–voltage (CV) curves to ensure optically-induced charge removal to reach its saturation at every photon energy, i.e. to exhaust all charge carriers available for optical excitation at a given photon energy $h\nu$.

2.3. Energy distribution of trapped electrons in a- HfO_2

EPDS measurements on a- HfO_2 samples were carried out at room temperature in the spectral range of $1.25 < h\nu < 6.5 \text{ eV}$ using an energy increment $\delta h\nu$ of 0.2 eV (with constant wavelength resolution of 10 nm) under +2V bias applied to the top metal electrode [37]. The exposure time per step was 1 h, which guarantees removal of at least 90% of charge available for de-trapping at every $h\nu$ as monitored by 200 kHz CV curve measurements. After analyzing an as-fabricated (pristine) MOS capacitor, the latter was injected by electrons or holes by applying a 20 ms long ‘write’ voltage pulse to the metal electrode. The pulse amplitude V_g was increased in steps of 1 or 2 V to achieve different trapped charge densities. Upon charging, the capacitors were kept in darkness for 48 h to allow for completion of thermal de-trapping before exposure to light starting from the lowest photon energy of 1.25 eV. After each illumination step, the charge variation in the insulating stack was monitored using CV curves. The corresponding charge density ΔQ_{stack} was calculated from the shift of the flatband point assuming a uniform distribution of traps across the HfO_2 layer. Finally, the SCD was calculated by normalizing the density of the re-charged centers to the spectral step width $\delta h\nu$. More detailed descriptions of these measurements can be found in the literature [37, 39–41]. Importantly, in the course of EPDS all captured electrons can be removed from the HfO_2 layer indicating that

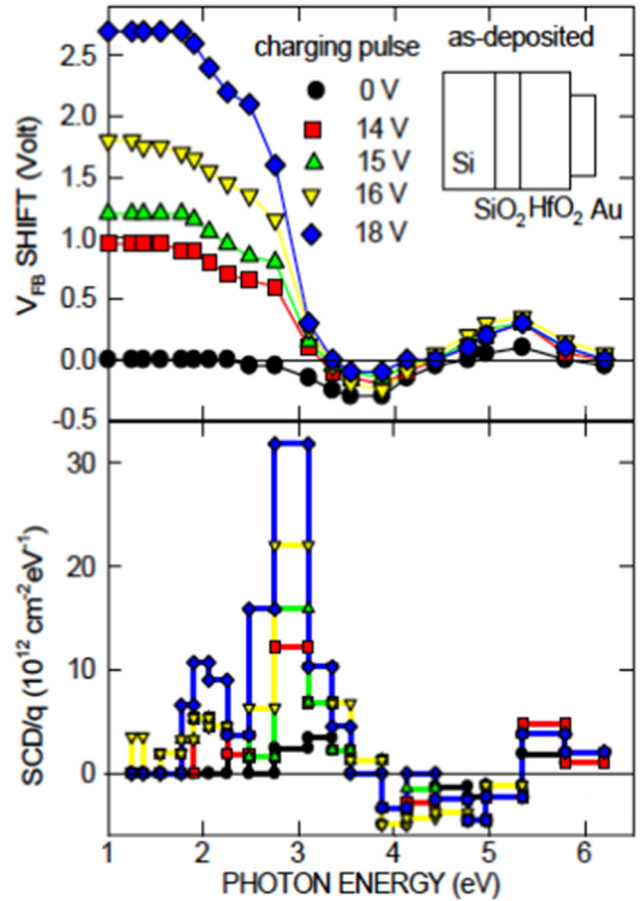


Figure 3. Illumination-induced flatband voltage variations (top) and the inferred SCD distributions (bottom) for samples with 19 nm thick HfO_2 insulator in pristine state and after injection of electrons by tunneling out of silicon upon applying the charging voltage pulse of the indicated amplitude. Reproduced from [58]. IOP Publishing Ltd. CC BY 3.0.

traps analyzed in this study represent the dominant source of electron trapping.

Figures 3 and 5 summarize the major experimental findings of EPDS measurements performed on the pristine and electron-injected samples with an as-deposited 19 nm thick HfO_2 insulator ($\text{HfCl}_4 + \text{H}_2\text{O}$ ALD precursor chemistry, for results on other films see [37]). Using the stepwise increase of photon energy $h\nu$, as illustrated in figure 2, and monitoring of the oxide charge by measuring the shift of flatband voltage (V_{FB}) on 200 kHz CV curves (figure 3, top panel) the illumination-induced charge variation can be converted to the SCD (figure 3, bottom panel) which reflects contributions of various electron processes to the oxide charging. One can distinguish three spectral ranges with different optically-excited electron transitions dominating the charge variation.

When $h\nu < 4 \text{ eV}$, electrons are excited from the energy levels E_t in the oxide gap (see figure 2) leading to a slight positive charging in the pristine HfO_2 sample or, in the charged samples, to the removal of electrons captured in HfO_2 upon electron tunneling injection. We note that in the electron-injected samples nearly all the trapped electrons can be de-trapped under illumination in the spectral range $h\nu < 4 \text{ eV}$. Interestingly, the charging spectrum of the pristine HfO_2 layer

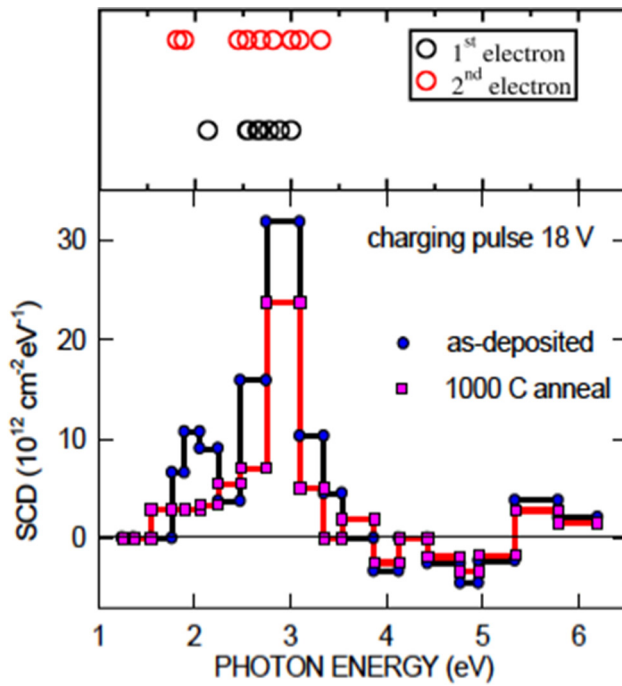


Figure 4. Top panel shows the results of theoretical calculations of electron, polaron and bi-polaron excitation energies to the mobility edge, indicated by hollow circles. Bottom panel compares inferred SCD distribution in the as-deposited sample and in the structure with HfO₂ layer crystallized by a 15 min anneal in N₂ at 1000 °C. Reproduced from [58]. IOP Publishing Ltd. CC BY 3.0.

fits in with that of the electron de-trapping, suggesting that the apparent positive charging of the as-deposited a-HfO₂ layer is also due to de-trapping of electrons from acceptor states partially filled by electrons during ALD growth of the oxide layer.

However, when $h\nu$ exceeds 4 eV, the sign of the illumination-induced charging changes to negative. The same effect has been observed earlier in the SiO₂/Y₂O₃ [40] and SiO₂/Al₂O₃ stacks [41]. This effect is related to the photo-injection of electrons from Si into the SiO₂ barrier layer and the subsequent trapping of these in HfO₂. The saturation negative charge density corresponds to the balance between trapping of the electrons photo-injected from Si and their de-trapping by the optical transitions from traps to the oxide CBM shown in figure 2.

Finally, when $h\nu$ reaches the threshold of intrinsic photo-conductivity of HfO₂ (the lowest bandgap $E_g = 5.6$ eV is close to that found in the monoclinic phase [57]) the generation of electron-hole pairs within the HfO₂ layer leads to the annihilation of trapped electrons [52]. Since the final charge state of the oxide stack after exposure to photons with $h\nu > 5.6$ eV is indistinguishable from that of the as-prepared (neutral) oxide stack, we conclude that there is no detectable density of hole traps or donor-type gap states present in the HfO₂ layers.

Since the excitation of electrons from the gap states into the HfO₂ CB represents the dominant (dis)-charging mechanism in the range $h\nu < 4$ eV, the SCD shown in the bottom panel of figure 3 directly reflects the energy distribution of the initial occupied electron states. The spectral plots in figure 3 clearly show that there are at least two components of the

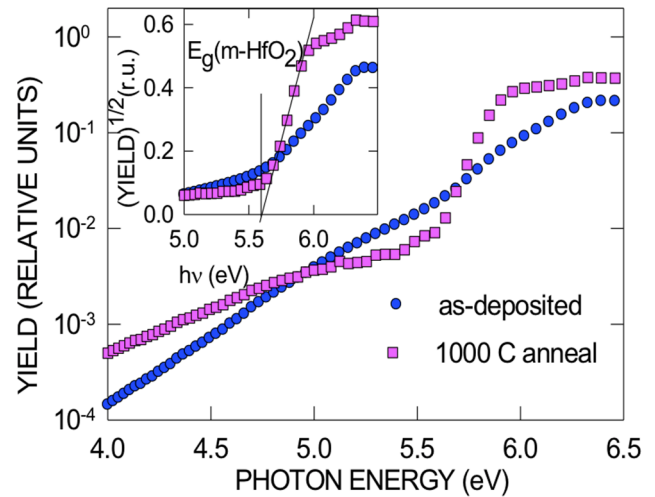


Figure 5. Photo-current yield spectra in the vicinity of the oxide photo-conductivity threshold measured in the as-deposited sample and after a 15 min anneal in N₂ at 1000 °C. The inset illustrates determination of the oxide bandgap E_g from the $(\text{Yield})^{1/2}$ - $h\nu$ plot. Reproduced from [58]. IOP Publishing Ltd. CC BY 3.0.

trapped electron density—at $2\text{ eV} < E_t < 3\text{ eV}$ and a deeper one at $3\text{ eV} < E_t < 3.5\text{ eV}$.

If these deep traps are an intrinsic property of amorphous films, changes in the film morphology should significantly affect the trapped charge. In particular, high temperature annealing is known to lead to crystallization of HfO₂ films. The morphology of samples subjected to the 15 min anneal in N₂ at 1000 °C is discussed in detail in [58]. Electron microscopy demonstrates that the annealed films still contain a significant volume fraction of a-HfO₂. Figure 4 compares the SCD spectra obtained on the as-deposited and annealed samples. Spectral dependence of the photo-conductivity (PC) yield defined as the photo-current normalized to the incident photon flux is shown in figure 5 for the as-deposited and annealed HfO₂ films. These curves indicate the spectral threshold of $E_g = 5.6$ eV corresponding to the monoclinic phase of HfO₂ after applying the high-temperature anneal [57]. The corresponding photo-excitation threshold (at around 5.9–6.0 eV, see the PC spectra of a-HfO₂ layers on Si₃N₄ [59]) or with admixture of Al, which prevents crystallization [60], can hardly be distinguished on the photo-conductivity spectra shown in figure 5 because it is energetically above that of the crystallized m-HfO₂ PC onset at 5.6 eV. In turn, from the SCD distributions shown in figure 4 one can conclude that the shallow component of the electron trap spectrum is strongly attenuated upon annealing of a-HfO₂. By contrast, deep traps with optical depths of about 3.0 eV are preserved.

These results suggest that the annealed film is most likely a mixture of amorphous and crystalline phases (a similar film is shown in figure 1(d)) and that change in morphology affects the energy distribution of electron traps. The observed similarity of the trapped electron energy distributions in a-HfO₂ layers grown using different Hf precursors or subjected to post-deposition annealing [37] suggests these centers should be intrinsic in nature. A feasible explanation is that these are oxygen vacancies. However, the calculations [37] showed

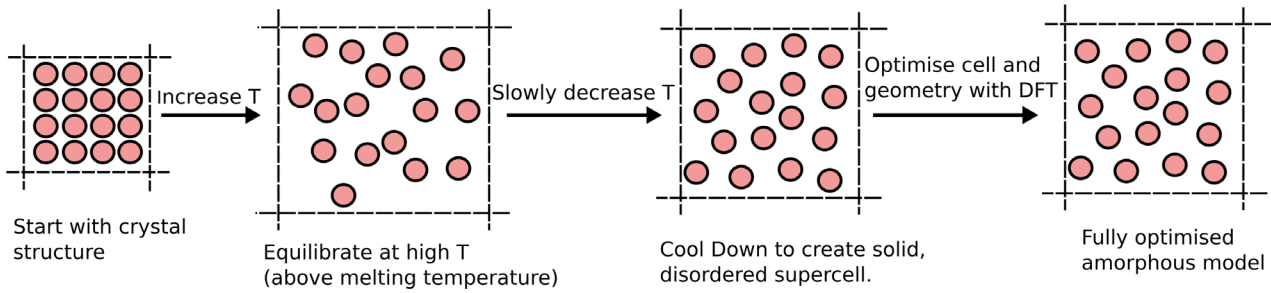


Figure 6. Schematic illustrating the melt/quench method for generating amorphous structures. Atoms are shown as filled circles.

that the charge transition levels of negative O vacancies are located higher in the bandgap than the peak at 2–3 eV below the mobility edge observed in figure 4. Therefore they cannot fully explain the negative charging of a-HfO₂ films. An alternative explanation suggested in [38, 58] is based on the idea that electrons can be trapped at structural features in amorphous network caused by disorder itself rather than absence of some atoms. Below we discuss how theoretical modeling is used to elucidate the nature of these electron traps in a-HfO₂ and predict the behavior of trapped charge in other amorphous oxides. We use this discussion to outline some of the challenges in modeling defects in amorphous materials.

3. Theoretical models of charge trapping

Scarce experimental data and lack of a general consensus on the electronic properties of amorphous films pose significant problems for theoretical predictions of the behavior of excess electrons and holes in these systems. On one hand, predicting electron or hole localization is a well-recognized challenge for DFT (see e.g. [61]). On the other hand, there are no established atomistic models of thin amorphous films grown on substrates. Since amorphous films are metastable, their morphology and atomic network structure strongly depends on deposition technique, anneal temperature, oxygen pressure and other factors [8, 62]. As shown above, under some conditions films can be a mixture of amorphous structures of different densities or co-present crystalline and amorphous structures. The film structure and morphology can significantly affect its electronic structure and charge trapping capacity. Below we briefly discuss theoretical methods used to model amorphous structures and calculate their electronic structures and properties.

3.1. Modeling of amorphous structures

Amorphous oxide films are experimentally grown using different methods: metal oxidation, film growth on semiconductor and metal substrates using different techniques, such as atomic layer deposition (ALD), pulsed laser deposition, chemical vapor deposition, molecular beam epitaxy, rf-sputtering, sol-gel dip coating, chemical synthesis of powders and other methods. The densities and atomic structures of produced samples strongly depend on the method and temperature of growth, anneal and other treatments. Different communities use different methods

of preparation and propose different ideas regarding the structure of these films. For example, the thermodynamic approach developed in [4] suggests that an amorphous structure of a thin oxide film grown on its metal substrate may be stabilized with respect to the corresponding crystalline oxide film on the substrate, up to a certain critical oxide-film thickness. This results from the absence of mismatch strain for the amorphous oxide film (in contrast to an epitaxial or semi-coherent crystalline oxide film). The critical oxide-film thickness when an initial amorphous oxide film transforms into a crystalline oxide film depends on the substrate orientation, temperature and metal-oxygen system under study [4]. However, density, thickness and morphology of oxide films strongly depend on the substrate material, the method of deposition and amorphous films well exceeding a critical thickness are grown on many substrates. The degree of crystallization depends on the subsequent thermo-chemical treatments (anneals), as has been observed for HfO₂, ZrO₂ [62], and other oxides [8], as well as on other factors, such as oxygen pressure [63]. Low oxygen pressure leads to the formation of oxygen vacancies, which may induce a decrease of the oxidation state of the metallic ions or a phase separation reaction in the oxide [63].

The fact that the morphology and atomistic structure of amorphous films are extremely sensitive to the sample preparation conditions makes simulation of these structures challenging. Atomistic models of amorphous films on substrates are still rare (see e.g. [64–67]) and 3D periodic bulk amorphous systems are simulated in most studies due to lower computational cost and the extra difficulties and uncertainties related to modeling interfaces. Using periodic cells is required in order to avoid border effects which may affect defect characteristics. However, this makes amorphous structures quasi-periodic and induces constraints on the structural relaxation accompanying defect creation.

The most popular method by far of ‘generating’ amorphous atomic structures is based on melting crystalline samples using 3D periodic boundary conditions and the subsequent cooling of the melt at different rates to low temperatures [8, 68], as outlined in figure 6. This method is based on the assumption that all liquids can be frozen into an amorphous state by fast cooling. The formation of glasses and amorphous solids from melt has been studied extensively, as reviewed in [69]. The concept of ‘fragility’ in glass-forming liquids based on the relationship between glass transition temperature and viscosity classifies liquids as strong and weak according to their glass-forming

ability [70]. Fundamental experimental and theoretical studies on liquids and glasses (see, e.g. [69, 71–73]) have shed light on the structure of fragile liquids, including ZrO_2 [74], HfO_2 [75], TiO_2 [76] and Al_2O_3 [77] discussed here. They are not glass-formers and can be frozen into a metastable amorphous phase from the melt. The experimental studies of molten oxides provide a wealth of information on their structure. The application of 3D periodic boundary conditions helps eliminate the nucleation of crystal phases, unless crystalline nuclei are deliberately introduced into melt. Cooling is usually unrealistically fast due to computer limitations and the cooling rate is rarely slower than 1 K ps^{-1} . In many cases, especially when quantum mechanical methods are employed, the cooling rate can be as large as 500 K ps^{-1} [8]. Since many oxides are either intermediate glass-formers or do not have a stable bulk amorphous phase, they tend to crystallize at low cooling rates. Further optimization of the volume and geometry of these structures and calculations of defect states are often performed using DFT and periodic models of a system. The obtained structures do not take into account the constraints and structural defects induced by interfaces with electrodes.

The most significant complication for modeling defects in amorphous oxides concerns variations in their local environment caused by structural disorder. Defects in the bulk crystalline phase formed at equivalent lattice sites have equivalent properties. By contrast, in amorphous structures all sites are different and any comparison of model parameters with experiment must involve statistical analysis of different configurations to estimate the probability of existence for each particular defect configuration and build a distribution of properties, e.g. formation energies. Due to high computational costs, more than several tens of configurations are rarely considered. Therefore, it is only feasible to talk about an approximate range in which a particular property can change rather than smooth distribution (see e.g. discussion in [78]).

Additional problems arise when modeling ‘polaron’ type trapping at intrinsic network sites. Polarons are quasi-particles formed in polar semiconductors and ionic crystals as a result of the interaction of extra electron or hole with the self-induced lattice polarization (so called self-trapping of polarons) [79]. The physical properties of the polaron differ from those of the band-electron; it is characterized by higher effective mass, optical absorption, EPR and specific temperature dependence of hopping mobility [80]. Localization of a small radius polaron in bulk crystal may take place at all equivalent lattice sites with equal probability. On the other hand, in amorphous structures all sites are different and deep charge trapping takes place only at some of the sites aided by structural disorder. The concentration of such sites is system specific and is difficult to predict *a priori*. At some of these sites carriers can be trapped spontaneously whereas trapping at others requires the carrier to surmount an energy barrier. For example, the predicted number of trapping sites where electrons can localize spontaneously in a-SiO_2 is about $4 \times 10^{19} \text{ cm}^{-3}$ [47]. Therefore, finding one such site with certainty in a periodic cell requires a cell size of around 1000 atoms. Other sites can also trap charge but in shallower states. Taken together these factors imply that simulations should be performed in the

largest periodic cells feasible for DFT calculations. However, different trapping sites have different trapping energies and related to these spectroscopic characteristics. To credibly predict *distributions* of properties, calculations in many models are required. Below we present examples of such approach to calculations for several oxides, starting from a-HfO_2 .

3.2. Methods for electronic structure calculations of amorphous oxides

The melt-quench method can be applied either by using so called *ab initio* molecular dynamics (MD) or by combining MD simulations using classical forcefields with the geometry optimization of obtained structures using DFT. The applications of the first approach to transparent conductive oxides has recently been reviewed in [8]. When reliable forcefields are available, the second approach is more efficient for producing many models of an amorphous structure and is used in our work.

In the monoclinic phase of HfO_2 shown in figure 7(A) Hf ions are 7-coordinated and equal numbers of O ions are 3- and 4-coordinated (see figure 7(D)). To understand the origin of the observed charging and SCD distributions in a-HfO_2 described above, 30 a-HfO_2 structures with densities of about 9.0 g cm^{-3} were produced using NPT classical molecular dynamics simulations and the inter-atomic potentials [81]. The temperature was linearly ramped to 6000 K at constant pressure and the structures were stabilized for 500 ps at 6000 K. The systems were cooled down from 6000 K to 0 K in 8 ns with a cooling rate of 0.75 K ps^{-1} . The Berendsen thermostat and barostat were used to control the simulations. We note that using an NPT ensemble is preferred when the density of amorphous film is unknown since one obtains a distribution of densities of the amorphous samples. These structures also exhibit wide distributions of bond lengths and atomic coordinations shown in figure 7(D). The details of these distributions depend on the size of the periodic cell and, for a-HfO_2 , the smallest cell which gives reproducible data contains 324 atoms [38].

All classical MD simulations predict the distribution of coordinations of O and Hf ions similar to the one shown in figure 7(D). The existence of two-coordinated O and five-coordinated Hf ions in a-HfO_2 samples plays a significant role in our further predictions. We note that low coordination of metal and oxygen ions has been observed experimentally in oxide melts [75, 82]. Further geometry optimization of the volume and atomic structures performed using DFT does not change the topology of the obtained structures. The optimized structures, however, have higher densities, in the range of $9.2\text{--}9.9 \text{ g cm}^{-3}$, with an average of 9.6 g cm^{-3} . The average Hf–O bond length is 2.1 \AA (ranging from 1.95 to 2.35 \AA) in a-HfO_2 which is very close to the Hf–O bond lengths in m-HfO_2 (around 2.1 \AA). The characteristics of excess electrons have been studied in ten 324 atom structures with densities in the narrow range of $9.5\text{--}9.75 \text{ g cm}^{-3}$.

The optimization of the volume and geometry of these structures and calculations of charge trapping sites in a-HfO_2 as well as other oxides discussed below have been performed

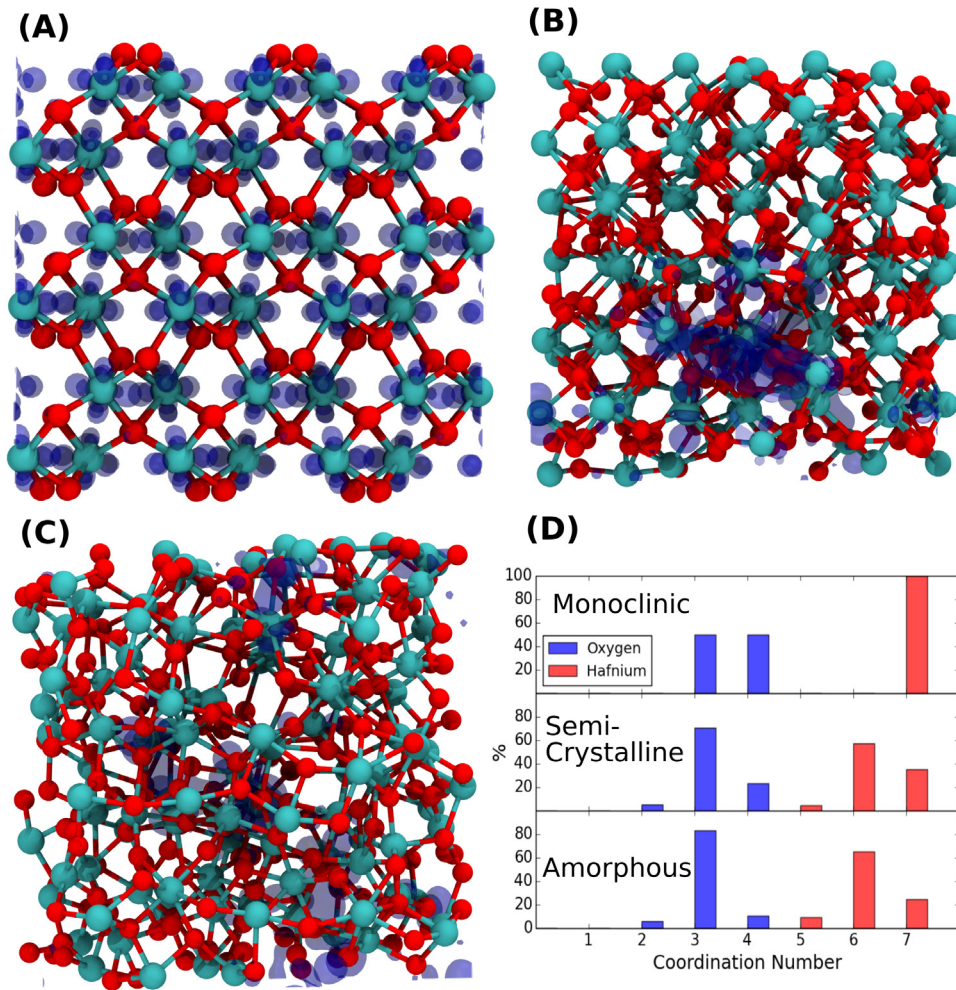


Figure 7. The geometry of a 324 atom HfO₂ cell in the monoclinic (A), semi-crystalline (B) and amorphous (C) phase. The transparent surface shows the iso-surface of the square modulus of the Kohn–Sham LUMO. In the monoclinic phase the state is delocalized across the Hf ions. In the semi-crystalline and amorphous phase the LUMO state is partially localized. (D) Shows the coordination numbers of O and Hf ions in the three phases.

using DFT implemented in the CP2K code [83, 84]. This code employs a Gaussian basis set mixed with an auxiliary plane-wave basis set [85]. The double- ζ Gaussian basis-sets [86] were employed on all atoms in conjunction with the GTH pseudopotential [87]. The plane-wave cutoff was set to 6530 eV (480 Ry). CP2K provides the efficiency essential to carrying out numerous geometry optimizations of defect and polaron structures in different charge states required for obtaining distributions of their properties. All geometry optimizations were performed using the BFGS optimizer to minimize forces on atoms to within 2.3×10^{-2} eV \AA^{-1} . The trapping energies of excess electrons and holes were corrected using the method of Lany and Zunger [88, 89]. Optical transition energies were calculated using the time-dependent density functional theory (TD-DFT) method as implemented in the CP2K code [90]. The crucial component of the computational scheme is a density functional, with a particular choice justified below.

One of the basic predictions of DFT calculations concerns polaron trapping energy. This is defined as a difference of total energies of the carrier in the perfect crystal or amorphous phase and the total energy after allowing structural relaxation.

If the carrier becomes localized and the energy of the localized state is lower than that of the initial state, the trapping energy is positive. This energy is equal to the thermal ionization energy of a polaron into the band and therefore serves as an indicator of polaron stability.

We note that in the one-electron picture [79], the polaron trapping energy is determined by the two main factors: increase of the kinetic energy of the electron or hole as a result of localization and gain in the potential energy due to the lattice polarization by the localized carrier. Tension between these two factors is illustrated below. In particular the kinetic energy change due to the carrier localization can be roughly estimated as a half of the width of the corresponding band (this estimate is valid for s-type bands as discussed in [91]). Therefore carrier localization is possible or energetically more favorable when the corresponding band (conduction band for electrons and valence band for holes) is flat. Large band dispersion hampers carrier localization.

It is well established that self-trapped polarons in oxide crystals typically have small trapping energies of the order of 0.1 to 0.3 eV [32, 92]. This means that even qualitative predictions of their stability are greatly affected by the choice of

the Hamiltonian. Applications of DFT to polaron states are plagued by the so-called self-interaction error which stems from the fact that the residual self-interaction in the Coulomb part of the DFT Hamiltonian and that in the exchange part do not cancel each other exactly for one electron [93]. This problem becomes particularly acute when local density functionals are employed to study electron localization in molecules [94, 95] and solids [61, 96, 97]. One of the popular fixes [97] concerns using so-called non-local functionals where a certain portion of the exact non-local exchange is admixed to one of the common (usually semi-local) density functionals [98]. This makes calculations much more computationally expensive but still does not fully solve the problem as one needs to determine the amount of Hartree–Fock exchange which needs to be included. A cheaper and more targeted approach is to adjust the U parameter in LDA + U or GGA + U calculations of polaron states [99]. Several flavors of this approach have been suggested over the years (e.g. [100, 101]), and it is still very widely used. The predictive power of these two approaches is again limited but they can be used very effectively in ‘test and predict’ mode where the parameters (e.g. the amount of HF exchange or the U value) are first fitted or ‘tuned’ to reproduce the established data and then the same parameters are used for predictive calculations. However, the transferability of these parameters between materials is quite limited.

A more consistent and now commonly used method is to correct the non-piecewise linearity of the total energy (E) with respect to (the continuous) electron particle number (N) in DFT systems [100, 102]. The linearity condition, where $d^2E/dN^2 = 0$, has been shown to be a property of the exact exchange-correlation functional by Perdew *et al* [103]. Local and semi local functionals deviate from the straight line behavior, instead showing curvature where $d^2E/dN^2 > 0$, while in HF theory the opposite behavior is observed and $d^2E/dN^2 < 0$. Lany and Zunger [100] proposed that, by enforcing the linearity condition, the self interaction energy of the electron or hole after addition is canceled by the energy of the wavefunction relaxation, allowing a more accurate description of localized states. Thus by tuning the appropriate parameter in either DFT + U [100] or hybrid functional calculations [102], the linearity condition can be enforced. It has not been demonstrated that satisfying this conditions is necessary for obtaining a correct description of electron localization. However, it has been observed that localization can indeed be achieved by tuning the parameters of the effective localizing potential [100] to satisfy the linearity condition. It should be noted that other specially tuned local functionals can provide electron or hole localization too (e.g. [101, 104]).

The calculations presented below use the range-separated non-local PBE0-TC-LRC functional [84]. This functional employs a truncated Coulomb (TC) interaction term and long-range correction for the exchange interaction (LRC). It is similar to the more commonly used HSE06 functional [105, 106] in that, unlike many other range-separated hybrid functionals, it uses short-range exact exchange and a long-range semi-local functional. We use the exchange interaction cutoff

radius as a variational parameter which is tuned to minimize a deviation of the functional from straight line behavior with the expectation that this will provide accurate predictions for electron and hole trapping energies (see [107] for detailed discussion). The obtained value of the exchange cutoff radius in HfO₂ is 4.0 Å. To reduce the computational cost of nonlocal functional calculations, the auxiliary density matrix method was employed [84].

3.3. Analysis of electronic structure of amorphous oxides

The square modulus of the one electron wavefunction at the bottom of the conduction band of m-HfO₂ is delocalized and periodic, as shown in figure 7(A). Structural disorder breaks the crystal symmetry and makes analysis of the electronic structure of amorphous material more complex. One can still use the electronic density of states as well as project it onto different atomic orbitals. However, the Kohn–Sham (KS) one-electron states are periodic only with the periodicity of the 3D supercell and may be partially localized within the supercell. Visual inspection of the electronic states at the CBM of a-HfO₂ shows partial localization onto hafnium $5d$ electronic states (see figure 7(C)).

The degree of localization of these states is characterized more quantitatively by calculating the inverse participation ratio (IPR) spectrum. This method takes advantage of the atom centered basis set used in CP2K to quantify the degree of localization of each eigenvector. It has often been used to characterize localization of vibrational and electronic states in amorphous solids (see e.g. [108–112]). Specifically, if the KS states are linear combinations of atom-centered basis functions, $\psi_n(\mathbf{r}) = \sum_i^N c_{ni}\phi_i(\mathbf{r})$, where ϕ_i are the basis functions, the IPR can be calculated as:

$$\text{IPR}(\psi_n) = \frac{\sum_i^N c_{ni}^4}{(\sum_i^N c_{ni}^2)^2}. \quad (1)$$

IPR can be calculated for each KS state in the valence band and conduction band. In this definition, IPR ranges between 0 and 1 and is very small for a delocalized KS orbital. For example, for a state fully delocalized across all basis functions with all of the coefficients of its basis functions equal to one another, the IPR will be $\text{IPR}(\psi_n) = \frac{1}{N}$, N being the total number of basis functions. Alternatively, localized KS orbitals will have high-valued IPRs.

A typical IPR spectrum of a-HfO₂ is shown in figure 8(A). One can see that there are localized states both at the CBM and at the top of the valence band of a-HfO₂. An extra electron or hole added to the system will inevitably occupy the lowest state in the conduction band or the highest state in the valence band, respectively. However, the tail states shown in figures 7(C) and 8(A) are only partially localized, which is reflected in the IPR values of around 0.02 to 0.07. For comparison, the IPR for fully delocalized states in the valence band has values between 0.003 and 0.0035. This corresponds to delocalization over approximately 300 basis functions. The delocalized states in the conduction band have a slightly higher IPR values of 0.004 due the lower number of Hf ions

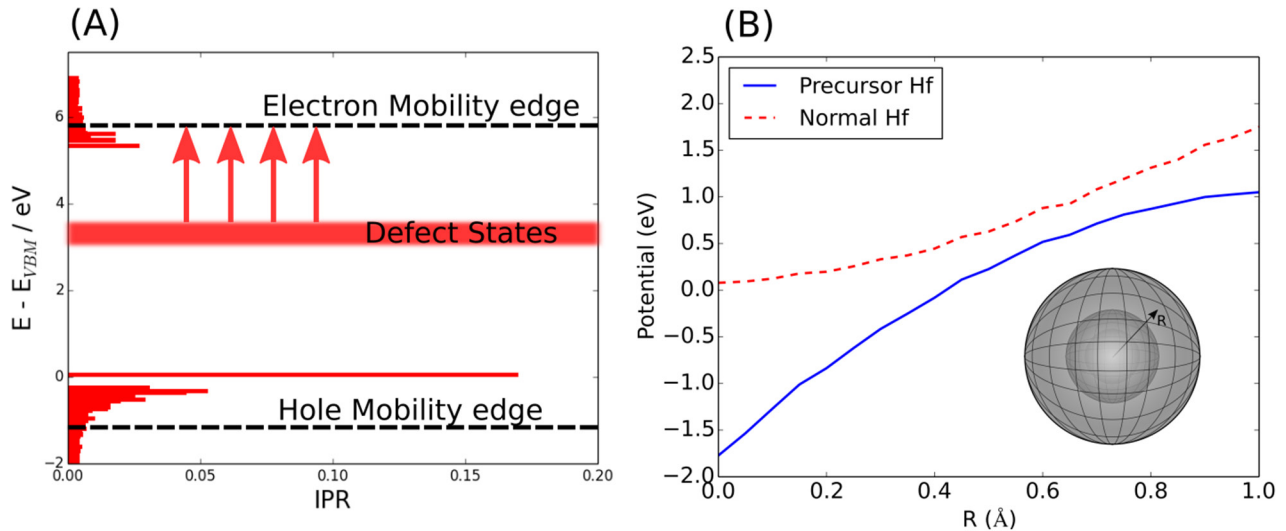


Figure 8. (A) Typical IPR spectrum of a-HfO₂. Large IPR values at the band edges indicate localized states and small IPR values correspond to delocalized states. The mobility edge position is estimated from the IPR spectrum. The position of the defect band of polarons and bi-polarons is also shown. (B) The Hartree potential (electrons + ions) as a function of radial distance R from Hf ions in a-HfO₂. The potential shown is the one experienced by an electron and shows that precursor Hf ions have a lower (more negative) Hartree potential. This helps to localize injected electrons onto precursor sites. The potential is averaged over the surface of the sphere with radius R , centered on the atom, which is then increased to show dependence on separation (as shown in the inset schematic).

in the system. Occupation of the tail states can lead to further electron or hole localization, as discussed in [111]. Therefore their existence is indicative of possible charge trapping. The fact that there are several states with high IPR values suggests that there can be several trapping sites in the cell. Analyzing the wave-functions responsible for large IPR values, one can identify sites in the amorphous structure where electrons or holes are likely to localize. However, finding the degree of electron or hole localization requires occupying these states and full geometry optimization.

Another important characteristic of the electronic structure of an amorphous solid, which can be deduced from IPR spectra, is the so-called mobility edge (ME). It is usually defined as a critical point where there is a transition between localized states, which do not contribute to the electrical conductivity of the system, and extended states, which can contribute to the electrical conductivity in disordered systems [80, 113, 114]. Using the IPR analysis, one can define ME as the onset of states with an IPR corresponding to delocalized states. At room temperature this definition is inevitably blurred by thermal activation of conductivity in partially localized states at the edge [80, 114]. We found the ME for electrons in the conduction band of a-HfO₂ to be approximately 0.5 eV above the LUMO KS state (see figure 8(A)).

4. Theoretical models of electron polarons and bi-polarons in a-HfO₂

Recent work [37] used EPDS to determine the energy distribution of trapped electrons with the electronic states in the band gap of a-HfO₂ films which were prepared using three different production-grade ALD methods. These measurements have demonstrated that at least two different components in

the electron trap spectrum are sensitive both to the deposition chemistry and to the subsequent thermal processing. On the basis of these observations, it has been suggested that these traps are associated with intrinsic defects in HfO₂, sensitive to the HfO₂ phase (amorphous versus crystalline). However, upon re-evaluation of the energy levels pertaining to the O vacancy in a-HfO₂, it has been concluded that O vacancies cannot be responsible for the charging behavior and that alternative models of electron trapping sites are required. These models will be discussed below and compared to the experimental traps spectra presented in the previous experimental section.

4.1. Electron polaron and bi-polaron in a-HfO₂

Theoretical calculations [38] have suggested that electrons can localize in energetically deep states at intrinsic structural traps in a-HfO₂. Trap sites can be either under-coordinated Hf ions or Hf ions with elongated Hf–O bonds, both of which are associated with a lowering of the electrostatic potential (for an electron). The average potential experienced by an electron near the precursor site and ‘regular’ site in a-HfO₂ is shown in figure 8(B). It shows that precursor Hf ions have a lower (more negative) Hartree potential. This helps to localize injected electrons onto precursor sites. We estimate that the density of such sites in a-HfO₂ is about $2 \times 10^{21} \text{ cm}^{-3}$. These structural characteristics can also be associated with the localized conduction band states shown in figure 8(A). We call the trapped states ‘polarons’ for brevity and in analogy with electron polarons in m-HfO₂, which are trapped only due to the lattice polarization. In a-HfO₂, however, electron trapping is facilitated by the fact that structural disorder creates precursor sites and allows for relaxation of the local atomic environment.

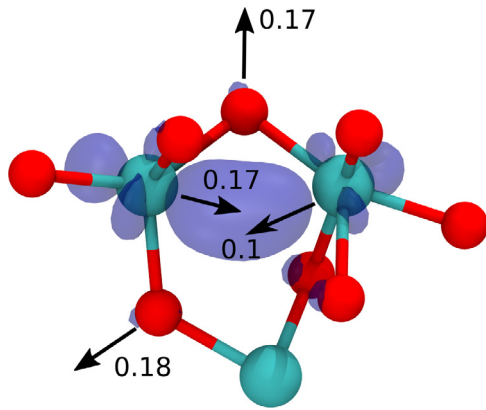


Figure 9. The electron polaron. Blue iso-surfaces indicate the electron density of the polaron state. Red spheres indicate oxygen ions and cyan spheres indicate hafnium ions. Black arrows show the directions of ionic displacements and their values are given in Å. Reproduced from [58]. IOP Publishing Ltd. CC BY 3.0.

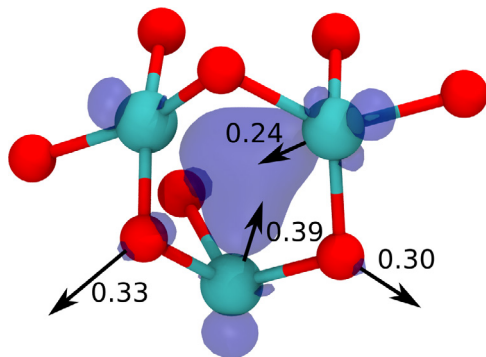


Figure 10. The electron bi-polaron. Blue iso-surfaces indicate the electron density of the bi-polaron state. Red spheres indicate oxygen ions and cyan spheres indicate hafnium ions. Black arrows show the directions of ionic displacements and their values are given in Å. Reproduced from [58]. IOP Publishing Ltd. CC BY 3.0.

In an electron polaron, a single electron is strongly localized over two or three Hf ions (figure 9). Upon polaron formation Hf–O bonds of these Hf ions are stretched outwards by 0.12 \AA , averaged over ten configurations. Multiple configurations of polarons were analyzed and the occupied KS states were found to be distributed between 1.6 and 2.5 eV below the bottom of the conduction band. These states are capable of trapping a second electron to form bi-polaron states (figure 10). The second electron is trapped over the same Hf ions, and so the bi-polarons show a similar distribution of electron density to the polarons. The bi-polaron formation is associated with further Hf–O bond stretching of, on average, 0.09 \AA . Polaron and bi-polaron states form a band of KS states shown schematically in figure 8(A). The width of this band is determined by the variation of local environments of electron trapping sites in the samples of similar density.

4.2. Calculated spectral charge density in a-HfO₂

In EPDS experiment, the electrons photo-ionized from the trap states in the gap should become mobile to be collected at the positively biased gate electrode. Therefore, to compare

with the experimental SCD data shown in figure 4, one needs to calculate a distribution of optical transition energies from polaron and bi-polaron states into the states at or above the electron ME in the conduction band of a-HfO₂, as illustrated in figure 8(A). Optical transitions from the charge trapping states into the conduction band were calculated using the TD-DFT method implemented in the CP2K code as described in [58]. These include transitions into the localized states at the bottom of the CB and into the delocalized states above the ME. The mobility edge is calculated for each a-HfO₂ structure and is typically found to be around 0.5 eV above the CBM. The distribution of energies shown in figure 4 corresponds to that of KS polaron and bi-polaron states with respect to the corresponding ME and agrees very well with the experimental spectrum. The intensities of the experimental peaks are determined mainly by the occupancy of the corresponding trap states after applying the high-field electron injection, which our statistics does not provide.

The agreement of the distribution of the calculated depopulation energies with the experimental SCD suggests that polarons and bi-polarons are likely candidates for explaining the negative charging of a-HfO₂ films. To check the consistency of this model with other experimental data, we investigated how thermal annealing affects the behavior of these traps.

4.3. Modeling the annealed samples

The experimental observations of the structure of annealed samples are described in [58]. A combination of transmission and scanning electron microscopies and grazing incidence x-ray diffraction on test structures of 25 nm thick oxide layers annealed at $1000 \text{ }^\circ\text{C}$ shows that the amorphous phase most probably remains present in HfO₂ films in significant volume fraction after the anneal. We should note that thinner HfO₂ layers or those deposited using carbon-containing precursors are more resistant to crystallization and may contain amorphous inclusions even at higher thermal budgets (see, for example, figure 1). For example, sub- 2 nm layers are commonly used as gate insulators in devices attempting to attain the equivalent oxide thickness below 0.5 nm [11, 48].

To create partially crystallized (pc) structures the same procedure as described above for amorphous structures was used, but a small part of the structure was frozen at perfect cubic HfO₂ lattice sites during both melt and quench. For smaller nuclei sizes, a significant part of the structure remains amorphous and the rest is crystallized (see figure 7(B)). The topology of pc-HfO₂ models obtained using classical MD simulations does not change significantly after full optimization with DFT. They have higher densities than the a-HfO₂ structures, ranging from 9.8 to 10.2 g cm^{-3} . One structure of each density has been chosen to perform further calculations. These structures are described in more detail in [58]. The band gap of pc-HfO₂ structures does not contain localized states due to the under-coordinated atoms and is equal to 6.0 eV on average. The IPR spectrum is similar to that of the a-HfO₂ cells and exhibits localization at the band edges and a conduction band ME approximately 0.5 eV above the CBM.

As in the case of a-HfO₂, we observe spontaneous localization of polarons and bi-polarons in deep states in each of the considered systems. However, the number of precursor sites is reduced as they are confined to the disordered regions in the structure. There is no electron trapping if the structure is fully crystallized in the cubic phase. We modeled several types of thermal fluctuations to facilitate electron trapping as discussed in [32, 115] but the extra electron remains completely delocalized after full geometry optimization. The formation of relatively shallow electron polarons has been predicted in monoclinic HfO₂ in [32].

The extra electron(s) in pc-HfO₂ localize on 6- or 7- coordinated Hf atoms. Among them, at least three oxygen neighbors have Hf–O distances longer than 2.16 Å. Extra electron(s) can also be localized on five-fold coordinated Hf atoms, which have longer Hf–O bonds. The average position of the KS level for the electron polaron in these structures is 2.4 eV below the conduction band minimum, whereas for bi-polarons it is 2.3 eV below the conduction band minimum. More than 90% of the electron spin density is localized on two Hf ions. The TD-DFT calculations of electronic excitations for several bi-electron structures show similar excitation energies to those reported in figure 4. Thus the anneal changes the SCD by reducing the number of the available electron trapping sites.

To summarize, the experimental and theoretical results discussed above provide first significant piece of evidence toward intrinsic nature of electron trapping in amorphous oxide films. Electron injection leads to the formation of localized states with optical ionization energies about 2–3 eV below the ME in the conduction band in ultra-pure HfO₂ films. The DFT calculations demonstrate that single and bi-electrons trapped at structural trapping sites in a-HfO₂ are likely candidates to explain the observed charge trapping. High temperature anneal of the films leads to their partial crystallization but still retains amorphous regions. DFT calculations demonstrate that electrons trapped in these regions have similar properties to those in amorphous samples but with a lower number trapping sites. These results consistently explain the nature of charge trapping in HfO₂ films revealed by EPDS spectra. The agreement of the experimental spectra and theoretical models suggests that low-coordinated metal ions in amorphous oxides can serve as deep electron traps in oxide films.

5. Theoretical models of polarons and bi-polarons in other amorphous oxides

The picture which emerges from the study of electron trapping in a-HfO₂ is that disorder creates electron traps associated with low-coordinated sites and elongated Hf–O bonds. These sites are capable of trapping up to two electrons. The electron trapping is accompanied by significant polaron-like distortion of the surrounding amorphous network creating deep states in the gap. Structural disorder serves as a natural source of ‘precursors’ for the formation of deep electron states [38]. Precursor sites are associated with the already-localized molecular orbitals at the band edges (as plotted in figure 7(C)). The high IPR valued molecular orbitals are found

to be localized onto certain structural motifs, e.g. under-coordinated Hf ions or Hf ions with elongated Hf–O bonds, both of which are associated with a lowering of the electrostatic potential (for an electron). As one can see in figure 8(B), the Hartree potential experienced by an electron near precursor sites is on average deeper than at ‘regular’ Hf sites in a-HfO₂, which makes them more favorable for electron localization.

How universal are these predictions for other amorphous oxides? Below we demonstrate that electron trapping can be expected in other amorphous oxides with *p* or *d* character of the conduction band minimum and that low-coordinated oxygen sites can universally serve as deep hole traps in amorphous oxides.

5.1. Deep electron polarons

Similar calculations to those described above for a-HfO₂ have been performed also for amorphous SiO₂ [47], Al₂O₃ [107], and TiO₂ [116]. In all cases the melt-quench method has been used to construct models of amorphous structures using classical forcefields accompanied by DFT geometry optimization. The densities and geometric characteristics of amorphous structures are in good agreement with the experimental data. However, there is a significant difference between the glass-former SiO₂ and the two other oxides. Amorphous SiO₂ forms a continuous random network structure of corner-sharing tetrahedra where Si remain 4-coordinated and O 2-coordinated. Disorder manifests itself in distributions of Si–O distances and O–Si–O and Si–O–Si angles [47]. On the other hand, a-Al₂O₃ [107] and a-TiO₂ [116] are similar to a-HfO₂ where the disorder is manifested in the distribution of coordinations of the Me and O ions and Me–O separations. However, when it comes to intrinsic electron trapping, the three materials behave very differently. Before going into further details we should note that comparison of the electron and hole localization in these different materials is meaningful only within a consistent set of computational methods. In all cases we used the PBE0-TC-LRC density functional where the exchange truncation radius has been tuned to minimize a deviation of the functional from straight line behavior, i.e. to satisfy the generalized Koopman’s condition.

5.1.1. a-SiO₂. The bottom of the conduction band in SiO₂, is mainly composed of *sp* Si states. The bottom of the conduction band in α -quartz has high dispersion [117] and no intrinsic electron trapping has been observed in α -quartz. The calculations [47] predict that electron trapping in α -quartz could happen over an energy barrier of 0.6 eV. However, in a-SiO₂ electron trapping may take place spontaneously at structural precursor sites which are wide O–Si–O angles exceeding 132° (see figure 13(a)) [47]. Using the theoretically generated amorphous structures of different sizes the concentration of such trapping sites was estimated at $4 \times 10^{19} \text{ cm}^{-3}$ [47]. Electrons can also trap at other Si sites with smaller O–Si–O angles, but that requires overcoming an energy barrier of up to 0.6 eV. An extra electron is localized on a Si site and the respective O–Si–O angle opens up to about 170° [47]

accompanied by a significant distortion of the surrounding network. The average gain in energy resulting from the barrier-less electron localization from the bottom of the conduction band of a-SiO₂ is 1.25 eV, ranging from 0.72 to 1.71 eV. The one-electron KS state occupied by the extra electron is located at about 3.2 eV below the bottom of the SiO₂ conduction band, indicating a deep electron trap. Further calculations and experimental measurements [118] have demonstrated that these electron traps can be responsible for the optical absorption bands peaking at 3.7 eV, 4.7 eV, and 6.4 eV in SiO₂ glass samples irradiated by electrons at 80 K.

Deep electron traps produced as a result of localization of one electron and the resulting network relaxation can also trap a second electron creating an even deeper bi-polaron state [119]. This is similar to the bi-polaron states in a-HfO₂ discussed above. When two extra electrons localize onto the same Si ion, the longest bond is stretched even further to an average of 2.1 Å while the O–Si–O angle widens to about 176°. The doubly occupied KS defect level is located at about 3.7 eV below the bottom of the conduction band on average, which is deeper than the singly occupied state. This is also reflected in the predicted position of the maximum of the optical absorption band of bi-polaron at 4.2 eV [119].

5.1.2. a-Al₂O₃. The bottom of the conduction band in corundum—crystalline Al₂O₃—has high dispersion of predominantly *s* Al states. No polaronic electron trapping in has been found in corundum. In a-Al₂O₃ the bottom of the conduction band is composed predominantly of *s* Al states with admixture of *p* states. The IPR analysis of a-Al₂O₃ electronic structure [107] reveals no localized states at the bottom of the conduction band. Thus, DFT calculations in a-Al₂O₃ so far failed to predict electron localization at structural precursor sites.

The results of *ab initio* molecular dynamics simulations [120] of oxygen defects in a-Al₂O₃ suggest that the structure and electronic states of oxygen vacancies and interstitials should strongly depend on the method of the oxide preparation. Vacancies created by O atom displacement from sites in a solid amorphous network produce states in the bandgap similarly to their counterparts in crystalline Al₂O₃. However, if vacancies are created in a melt, which is then cooled down, their signatures disappear and they blend into the frozen melt structure [120]. Since a-Al₂O₃ films are rarely produced from the melt and are grown using atomic layer deposition, sputter deposition and other methods and then annealed, experimental defect signatures could help to verify this model and shed light on the structure reorganization upon anneal.

The negative charging of a-Al₂O₃ films and the distribution of defect levels have been measured using EPDS in [41]. These films were grown by ALD at 300 °C and a post-deposition anneal was carried out immediately after deposition. The results of recent calculations [121] demonstrate that both the charging process and the energy distribution of traps responsible for negative charging of a-Al₂O₃ films [41] can be understood assuming that the negatively charged O_i and V_{Al} defects are nearly compensated by the positively charged H_i, V_O and Al_i defects in as prepared samples. Following electron

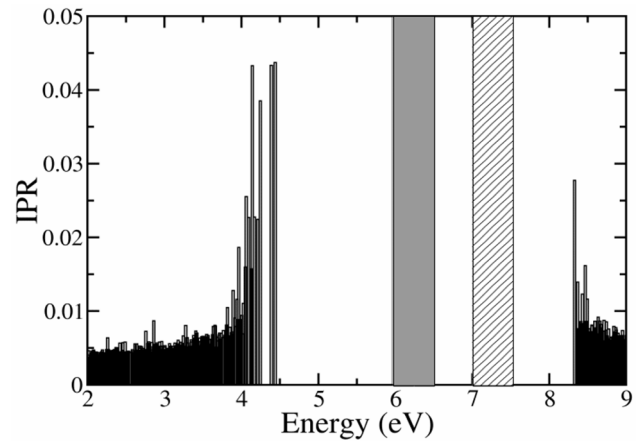


Figure 11. (a) The IPR spectrum of a-TiO₂. Large IPR values at the band edges indicate localization of the state and small IPR values indicate delocalization. The mobility edge position can then be estimated from the IPR spectrum. The energy ranges for the electron(hole) polarons in ten amorphous structures are shown by solid(hatched) gray areas.

injection, the states of Al_i, V_O or H_i in the band gap become occupied by electrons and sample becomes negatively charged. These results suggest that under the ALD growth conditions oxygen defects in a-Al₂O₃ still retain their properties.

5.1.3. a-TiO₂. The bottom of the conduction band in crystalline TiO₂ is dominated by Ti *d* states [122, 123]. Small electron polarons in rutile (r)-TiO₂ have been studied experimentally [2, 124–128] and theoretically using DFT [129–136]. The calculations show that the total energy of self-trapped localized electrons is lower than that of delocalized electrons in the conduction band by about 0.9 eV [134] or less. In anatase, holes are trapped in deep hole polaron states [130, 137] but electron polarons are metastable, which has been confirmed by DFT results [130, 131, 138].

The IPR spectrum of a-TiO₂ in figure 11 shows localization of KS states at the bottom of the conduction band and top of the valence band [116] and structural motifs responsible for these states can be considered as precursor sites for carrier localization (see also [139]). These motifs typically include under-coordinated Ti(O) ions and elongated Ti–O bonds, as observed experimentally in the melt [76] and amorphous phase [29]. At the original a-TiO₂ geometry, an extra electron exhibits some preferential localization on a few Ti atoms. After the geometry optimization the degree of localization increases to about 86% on one Ti atom. There is no barrier for creation of these localized states. The average degree of electron localization out of ten a-TiO₂ models treated in [116] is ~90% on one Ti atom and deep KS states are created in the bandgap by the trapped electrons. They are indicated by the gray area in figure 11 with the width of the area corresponding to the range of distribution of occupied electron states. These are located at ~2.0 eV below the bottom of the conduction band ranging from 1.8 to 2.5 eV (see figure 11).

Due to the wide distribution of coordination numbers and bond lengths in the amorphous models, there exists a number

of precursor sites where the electron can be trapped. These correspond to several peaks in the IPR spectrum in figure 11. These trapping sites can be explored either by adding more electrons to the cell or by inducing structural distortion near precursor sites to facilitate the electron localization. The resulting electron polarons trap at different depths in the band gap and form a range of KS states shown in figure 11. This behavior differs from the case of rutile and anatase where electron polarons form more shallow states on regular Ti sites.

The average electron trapping energy in ten a-TiO₂ models is about 0.8 eV with a wide distribution ranging between 0.6 eV and 1.1 eV. This range corresponds to the width of the gray area in figure 11. The relatively large trapping energy suggests stability of localized electrons at room temperature. Further analysis of the trapping sites demonstrates that the extra electron localized either on the elongated Ti–O bonds or on the under-coordinated Ti atoms. There is a noticeable structural distortion after the electron localization similar to a-HfO₂ [38] with the Ti–O bonds elongated by ~ 0.1 Å on average. The IPR analysis demonstrates that in eight of the ten structures there is at least one precursor site in 270 atoms periodic cells for an electron polaron to trap. One of the two remaining structures has two precursor sites and the other one has three precursor sites. The smallest distance between these precursor sites is ~ 0.8 nm.

Thus structural disorder in amorphous oxides with low dispersion of *p* and *d* character at the bottom of the conduction band facilitates strong electron localization on under-coordinated sites with elongated bonds. By contrast, electrons in *s* states in oxides, such as ZnO [140] and Al₂O₃ [141], have high dispersion and are likely to remain mobile even in the amorphous phase. However, this may not always be the case, as suggested by the example of InGaZnO₄—a prototype In-based amorphous oxide semiconductor [142]. The lowest conduction band states of amorphous InGaZnO₄ are mainly characterized by the In-*5s*-like atomic orbitals, and their effective overlap through the In atomic sites results in a low electron effective mass. Ionic oxides including heavy post transition metal cations with an electronic configuration $(n-1)d^{10}ns^0$, where $n \geq 5$, have been proposed as candidates for good amorphous transparent conductors in [143]. However, one or two electrons have been predicted to trap at low-coordinated In sites in InGaZnO₄ pinning the Fermi level in heavily n-doped samples [142]. This example demonstrates that strong perturbation induced by disorder can in some cases facilitate localization even on highly dispersed *s* states.

5.2. Deep hole polarons

The top of the valence band of most oxide wide gap semiconductors and insulators is composed predominantly by lone-pair O *2p* states and has low dispersion. Therefore hole polarons are known to localize in many crystalline oxides forming relatively shallow states bound to impurities or self-trapped at intrinsic sites (see e.g. [92, 100, 144–146]). DFT calculations of hole trapping in crystalline phase monoclinic HfO₂ and corundum Al₂O₃ demonstrate that holes can trap predominantly on one oxygen site with trapping energies of

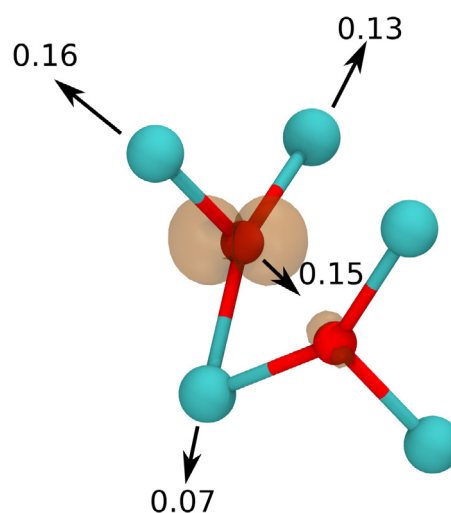


Figure 12. The hole polaron in a-HfO₂. Red iso-surfaces indicate the square modulus of the hole state. Red spheres indicate oxygen ions and cyan spheres indicate hafnium ions. Black arrows show the directions of ionic displacements and their values are given in Å. Reproduced from [58]. IOP Publishing Ltd. CC BY 3.0.

around 0.2 eV. In rutile TiO₂ no hole trapping was found, but in anatase the calculations [116] predict the hole trapping with the trapping energy of ~ 1.1 eV.

Much less is known on how disorder in amorphous oxide films affects the character of hole localization. The IPR spectrum of a-HfO₂ in figure 8(A) shows a strong peak at the top of the valence band as well as several other peaks deeper in the band, which suggest that spontaneous hole localization can be more prominent than electron localization in this sample. This is indeed confirmed by full geometry optimization. Perhaps the best studied are self-trapped holes in a-SiO₂ [147] which are stable at temperatures below 180K. Theoretical calculations [148, 149] support the existence of hole states localized on one and two O ions (so-called STH1 and STH2 states [147]).

Recent calculations in a-HfO₂ [38], a-Al₂O₃ [107] and a-TiO₂ [116] have demonstrated that holes can form deep single- and bi-polaron states in these materials, which should be stable even at room temperature. These calculations have been performed using the same amorphous structures and DFT methodology as discussed above for the electron localization. In the amorphous phase, intrinsic trapping sites at under-coordinated O ions cause deep hole trapping in all three materials with trapping energies exceeding 1.2 eV ranging between 0.9 eV and 1.6 eV, making these states likely candidates for positive charging in oxide films. The character of spin density distribution and displacements of the nearest neighbor Hf ions around a trapped hole in a-HfO₂ is shown in figure 12. One can see that the hole is predominantly localized on one O ion.

The formation of hole bi-polarons in a-HfO₂ can happen spontaneously and some of them have high binding energies, exceeding 1 eV. On the other hand, in a-Al₂O₃ the formation of hole bi-polarons requires overcoming an activation barrier and binding energies remain small or even become negative [150]. The more ionic character of chemical bonding in Al₂O₃ than in HfO₂ results in the much weaker bonding in O–O dimer

configurations characteristic to bi-polarons. We note that the formation of double-hole-induced oxygen dimerization in other transition metal oxides, such as TiO_2 , V_2O_5 and MoO_3 has been predicted by DFT simulations in [151]. Bi-polarons do not create unoccupied states in the band gap and are EPR inactive, which makes them difficult to detect experimentally using spectroscopic techniques.

To summarize, on the basis of these results one can expect trapping of positive charge to be much more severe and stable in amorphous films rather than in crystalline samples.

6. Defect formation facilitated by electron and hole trapping

It is often assumed that new oxygen vacancy–interstitial ion pairs are generated in the oxide as a result of stress application where strong electric field weakens Me–O bonds [152, 153]. However, the Frenkel defect (FD) pair formation energies in m-HfO₂ have been calculated to be 8.0 eV for formation of the neutral pair, 7.3 eV for the pair of singly charged defects, and 5.8 eV for the pair of doubly charged defects [154] and similarly high values are known in other oxides. Therefore activation barriers for formation of these defects are even higher and are unlikely to be reduced significantly as a result of bias application. It has been noted that, depending on the Fermi level position, formation energies of FDs in monoclinic HfO₂ can become thermodynamically much lower by introducing electrons into the system [155].

Similar ideas have been developed in [156] where DFT calculations have been used to investigate whether the formation of FDs can be aided by electron injection into perfect m-HfO₂ and at pre-existing O vacancies. Electrons injected into the conduction band can form polarons [32] or trap at pre-existing O vacancies [157]. The results of calculations in [156] demonstrate that neutral oxygen vacancies and charged interstitial O^{2−} ions can be produced in m-HfO₂ under electron injection conditions even at zero bias. Although the formation energy of a pair of charged defects V²⁺ and O^{2−} is the lowest, these defects interact strongly due to the Coulomb attraction and forming them via O^{2−} ion displacement from a regular lattice site proves impossible as the nearest neighbor pairs recombine back. When one extra electron is involved, a V¹⁺ is formed and the Coulomb attraction with the nascent O^{2−} interstitial ion is weaker. However, the nearest neighbor Frenkel pair is unstable and recombines [156]. Two extra electrons can neutralize a positively charged V²⁺ oxygen vacancy, thus preventing its recombination with the O^{2−} interstitial oxygen in the Frenkel pair. The O^{2−} interstitial ion can then diffuse away with a (0.5–0.7) eV activation barrier. The barrier of 2.0 eV to FD formation by this mechanism is much lower than when no electrons are involved. This barrier was shown to be lowered down to 1.25 eV by forming a defect pair next to a pre-existing neutral oxygen vacancy. The pre-existing vacancy acts as an electron trap, and the di-vacancy that forms is stable, further lowering the formation energy of the defect. Furthermore, since the binding energy per vacancy in oxygen-vacancy aggregates increases as the aggregate grows,

it is likely that the formation of a NN FD pair next to a larger vacancy aggregate will require even lower formation energy. Bias application can further lower the barriers for FD pair formation.

This mechanism requires a concerted action of two electrons. The probability of such process is low but increases as the current density increases. The fact that this mechanism produces charged O ions is in agreement with voltage-driven ion migration in bipolar devices. Charged interstitial ions are likely to be the fastest diffusing oxygen defect in m-HfO₂, especially under high positive bias and electron injection conditions. The role of charge injection in FD formation and the diffusion of O ions in m-HfO₂ has been studied in [158] and confirmed a significant lowering of the activation energy to defect formation.

These results prompted us to look into similar effects in amorphous HfO₂ and SiO₂. Bi-electron traps in amorphous phases are much deeper than polarons in m-HfO₂ and electrons can be injected directly into these states from electrodes. Extra electrons in a-HfO₂ are localized around two or three Hf atoms. However, the formation of bi-polarons causes strong Hf–O bond weakening manifested in significant (about 0.3 Å) ionic displacements (see figure 9). The KS energy levels of the polaron states in a-HfO₂ are much deeper than in m-HfO₂. For example, the electron bi-polaron in a-HfO₂ induces KS states which are, on average, 2.2 eV below the bottom of the conduction band. Thermal activation of these bi-polarons may cause FD formation in a-HfO₂ [159]. However, FD formation energies are higher in the amorphous phase than in m-HfO₂.

This stems from the qualitative difference between the FD formation in a-HfO₂ as compared to m-HfO₂. In the crystalline case, electrons are injected into the conduction band and form shallow polarons and bi-polarons with states about 0.3 eV below the conduction band. Therefore there is a significant energy gain due to the localization of these extra electrons in an oxygen vacancy in the process of FD formation (however, the cross-section for formation of bi-polarons is rather low). In the amorphous case, however, the second electron can tunnel directly into the single electron polaron state and the FD formation takes place from the already localized bi-polaron state and the initial configuration thus has a lower energy. As a result, the defect formation energies in the amorphous case are greater than in the crystalline case. The lowest energy barrier to forming a nearest neighbor FD pair was calculated to be 1.9 eV [159] and can be further reduced as a result of bias application.

It turns out that a similar mechanism of FD creation can take place also in a-SiO₂ [119]. The calculations demonstrate that electron trapping at precursor sites and formation of bi-polarons results in weakening of Si–O bonds, which can be broken upon thermal activation, creating an O^{2−} interstitial ion and a neutral O vacancy (see figures 13(b) and (c)). O^{2−} interstitial ions can easily diffuse through the oxide and in devices are guided to the positive electrode by the electric field. However, the predicted barrier for FD creation in a-SiO₂ is much lower than in a-HfO₂ and is on average around 0.7 eV [119].

The energy cost of creating an oxygen vacancy depends greatly on the local environment. Not only is there a spread of formation energies owing to the disorder, but pre-existing vacancies can affect both the position and the barrier for forming a new vacancy. For instance the distortion of the surrounding network caused by electron trapping in a vacancy can create another precursor site for electron trapping nearby and the aggregation of several vacancies can distort the surrounding network and enhance the local electric field, leading to creation of new vacancies. In this way the number of O vacancies will grow with increasing film degradation which leads to a feedback process and eventually to dielectric breakdown. Recent calculations [160] demonstrate that the creation of additional wide O–Si–O angle intrinsic electron traps is correlated with the local strain induced by the presence of pre-existing O vacancies. Trapping two extra electrons at a vacancy in a-SiO₂ leads to a strong distortion of the surrounding amorphous network [161]. As the size of the O vacancy clusters increases, the likelihood of creating another vacancy nearby increases as well. Single vacancies have a 25% chance of inducing a wide O–Si–O angle intrinsic electron trap when charged, divacancies have a 50% chance, and tri-vacancies are the most likely to create a nearby intrinsic trap with a 77% chance [160]. This sequence of events is schematically illustrated in figures 13(d)–(f) for the creation of the second vacancy at the pre-existing O vacancy as a result of trapping of two extra electrons from the electrode.

The microscopic mechanisms responsible for the creation of O vacancies and the related correlation effects strongly influence the statistics of dielectric breakdown. The feasibility of the breakdown mechanism based on FD creation in a-SiO₂ facilitated by electron injection has been investigated in [153]. The multi-scale model proposed in this work self-consistently describes the main physical mechanisms in SiO₂ under electrical stress using the parameters generated by DFT calculations of defect characteristics and FD generation mechanisms [119]. Charge transport was modeled self-consistently by including conduction mechanisms, such as direct tunneling, defect assisted multi-phonon trap-assisted-tunneling (TAT) [162], and carrier drift across either the conduction/valence band and defect sub-bands. The defect properties determined from DFT were used in the calculation of TAT current contributions to account for electron–phonon coupling. Wide O–Si–O bond angle precursors were randomly generated for every simulated sample with a uniform spatial distribution and with energy parameters within the ranges reported in [119]. The time-dependent dielectric breakdown distributions were simulated at different stress voltages. The good agreement between simulations and experiments obtained in [153] at different biases confirmed that this mechanism could be responsible for the degradation and dielectric breakdown in silica.

These results suggest that localization of injected electrons in amorphous oxides can facilitate creation of FDs. However, much less is known about whether similar mechanisms can work under hole injection conditions. According to the results presented above, hole localization is much more likely in

amorphous oxides. The calculations performed in [159] demonstrate that formation of the hole bi-polaron in a-HfO₂ facilitates the formation of stable V²⁺ vacancies and interstitial O atoms, both of which can diffuse relatively quickly. The effect of electron and hole injection on the creation of FDs has also been considered in rutile TiO₂ [163]. DFT calculations demonstrate that the activation barrier to formation of an O vacancy defect can be reduced by the trapping of holes which may be injected from an electrode.

7. Effect of charge trapping on functionality of oxide films

Developing reliable methods for identifying and analyzing electron traps in thin oxide films is of utmost importance for eliminating or limiting their impact on the performance of a growing range of electronic devices. For example, it has recently been suggested that ferroelectricity of both doped [164, 165] and pure [166] HfO₂ may offer new paths for the application of HfO₂ films, including memories [167] and high sub-threshold slope transistors [168]. However, the positive bias-temperature instability driven by electron injection into oxide films limits the gate oxide scaling in metal-HfO₂-Si transistors [48, 49, 53, 54]. Furthermore, in flash cells, electron trapping in the integrated HfO₂ insulator degrades the program/erase window, retention, and endurance [50, 169].

Though electron trapping in the insulating layer is primarily seen as a degradation factor impairing charge carrier mobility and causing instability of the threshold voltage in MOS transistors, in some applications the presence of charge might be desirable. The example of a-Al₂O₃ layers with a significant density of fixed negative charge was mentioned in the Introduction. They are used to achieve electrostatic passivation of silicon solar cells [18–20]. Introducing significant band bending at the silicon side of the Si/a-Al₂O₃ interface leads to reduction of the surface recombination, thus improving the solar cell efficiency. Formation of negative charges in alumina is seen as a result of electron transfer from silicon to the oxide traps thought to be either oxygen interstitials [170] or aluminum vacancies [18]. However, these trapping site models can hardly explain the thermally-activated increase of the negative charge observed when annealing a-Al₂O₃ layers on Si at temperatures below 500 °C [171] which are insufficient for alumina crystallization.

Another recent example of the benign influence of electron trapping on the functionality of amorphous oxide is provided by a-TiO₂ films which are used to fabricate highly non-linear cells in resistive memory arrays [172]. Electron transport across oxide films critically depends on the presence of electron traps [173] which modify barrier height at one of the amorphous oxide interfaces [174]. Polaronic origin of these traps (as opposed to the routinely used oxygen vacancy hypothesis) may explain effective current modulation observed in a-TiO₂/a-Al₂O₃ stacks [172] since deep electron polaron states are not found in alumina.

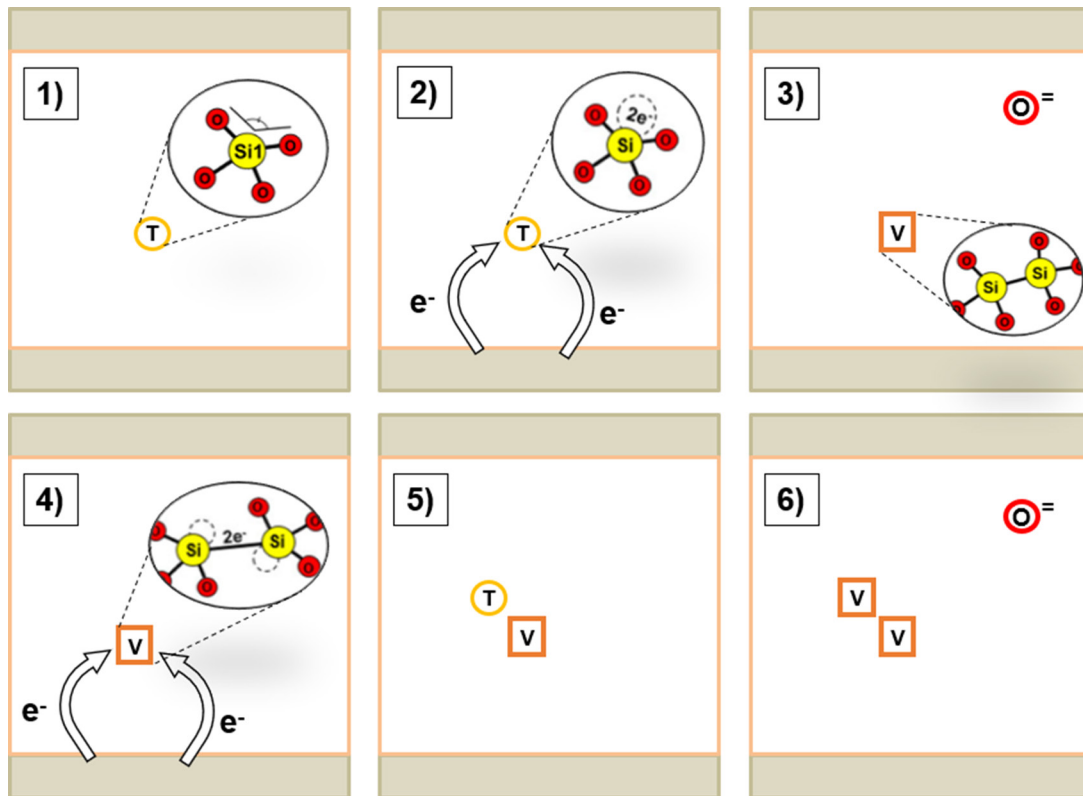


Figure 13. Schematic of the proposed degradation mechanism in a-SiO₂ facilitated by electron injection. (1) Shows an electron trap in amorphous structure; in (2) this trap captures two electrons from the substrate, which results in the formation of FDs in (3). In (4) two electrons are trapped on O vacancy; this creates an electron trap nearby in (5) and the formation of another O vacancy and interstitial O²⁻ ion in (6). Further trapping of electrons results in the formation of more O vacancies nearby, as discussed in [160].

Finally, the violation of electro-neutrality at interfaces of amorphous oxides with metals due to formation of electron polarons may become an important factor affecting the effective work-function of a metal by creating a double electrical layer. As a result of this oxide-sensitive contribution to the interface energy barrier, the effective work-function of a metal at the interface with the oxide will differ from the work-function measured in vacuum. Experiments indicate that this difference may exceed 0.5 eV leading to the formation of large built-in voltages, significantly affecting distribution of electrostatic potential in device structures [175]. Furthermore, in the case of co-presence of amorphous and crystalline phases in the oxide films the differences in polaron energies may lead to laterally non-uniform interface charge distribution, resulting in non-uniform interface barrier—the effect also confirmed by experimental observations [175].

8. Outlook

We have provided an overview of recent progress in understanding of the physics of electron and hole trapping in amorphous oxide films and its impact on the functionality of electronic devices. The picture emerging from theoretical simulations suggests that there is a trend for considerably deeper electron and hole trapping in amorphous oxide films than in crystalline films. Furthermore, the structure of amorphous oxide films can evolve as a result of charge carrier

trapping/de-trapping and ensuing defect creation. However, it needs to be recognized that it is difficult to confirm theoretical predictions by direct experimental observations. Proving the relevance of these predictions to charging processes in real device-relevant structures probably represents one of the biggest experimental challenges in this field. Nevertheless, we have presented the results available for the best-studied case of a-HfO₂ films and discussed issues associated with theoretical modeling of charging phenomena. Although the accuracy of DFT calculations of materials' properties is improving, their ability to predict electron and hole localization strongly depends on the density functional used. Therefore comparison of predicted properties with experiment is paramount and we have demonstrated several examples where this has been possible to achieve.

Modeling of electron localization in disordered solids represents strong stimulus for atomistic simulations. One of the most formidable challenges here concerns reliable prediction of metastable structures of non-glass-forming amorphous materials. Here we discussed only one of the modeling methods used in this field—the melt and quench method of bulk 3D structures. More realistic approaches should also include effects of interface strain, which is one of the main factors in stabilizing metastable structures of thin films. Other methods, such as the activation-relaxation technique [176, 177], have been applied to construct amorphous oxide structures [178] but did not get much traction so far. The mentioned

metastability of amorphous structures raises many interesting questions regarding the nature of defects, especially vacancies as they are difficult to distinguish from low-coordinated sites [142, 176]. Creation of new defects as well as electron trapping and de-trapping lead to distortions and irreversible structural changes in amorphous network structures which are genuine in some cases and may prove artifacts of simulations in others [78]. Low probability of charge trapping poses significant challenges for accurately predicting the concentrations of trapping sites and distributions of distances and trap energies. This is not only a computational problem, which can be overcome by calculating more structures, but requires much more detailed analysis of irreversible structural transformations caused by charge trapping [78]. Carrier localization strongly affects their mobility in disordered solids as have been reviewed in many publications [179, 180]. The deep polaron states predicted in amorphous oxide films are typical for variable range hopping [179]. However, bi-polaron formation, competition with defect formation and wide distributions of hopping distances and trapping energies make modeling of the carrier mobility in these systems very complex.

Besides their importance for improving performance and functionality of oxide films discussed here, our results should be seen in a broader context because variability of the cation coordination represents an intrinsic property of many other amorphous oxides [25–29], as well as nanocrystallites widely used in photo-catalysis. In particular, electrons in oxides with *p* and *d* character of the CBM often have low dispersion and are particularly prone to charge localization. Furthermore, electrons and holes can behave very differently in the bulk and at surfaces of these materials. A good example is given by TiO₂ where electron polarons are very shallow in the bulk [124] but become much deeper at surfaces and in nanocrystals where the atomic coordination is reduced and bonds are strained [128, 181]. Therefore, one may expect the mechanism of electron self-trapping to be relevant to a broad variety of other non-glass forming insulating oxides. As a concluding remark, it should be added that this charge trapping does not require any kind of ‘damage’ of the oxide network and occurs naturally, due to intrinsic structural properties of amorphous solids.

Acknowledgments

MK and ALS are grateful to the World Premier International Research Center Initiative (WPI) sponsored by the Ministry of Education, Culture, Sports, Science and Technology (MEXT), Japan for financial support. We gratefully acknowledge funding provided by EPSRC under grants No. EP/K01739X/1 and EP/P013503/1 and by the Leverhulme Trust RPG-2016-135. Computer facilities on Archer service have been provided via the UK’s HPC Materials Chemistry Consortium (EPSRC Grant No. EP/L000202). The authors thank the Supercomputer Center, the Institute for Solid State Physics, the University of Tokyo for the facilities and the use of the SGI Altix ICE 8400EX. The authors are grateful to G Bersuker, S Bradley, J Cottom, O Dicks, M Koleini, L Larcher, K P McKenna, D Mora Fonz and A Padovani for valuable discussions.

ORCID iDs

Jack Strand  <https://orcid.org/0000-0002-4603-6151>

Valeri V Afanas’ev  <https://orcid.org/0000-0001-5018-4539>

Alexander L Shluger  <https://orcid.org/0000-0002-2488-0896>

References

- [1] Dearnaley G, Stoneham A and Morgan D 1970 *Rep. Prog. Phys.* **33** 1129
- [2] Austin I and Mott N 2001 *Adv. Phys.* **50** 757–812
- [3] Diebold U, Li S C and Schmid M 2010 *Annu. Rev. Phys. Chem.* **61** 129–48
- [4] Reichel F, Jeurgens L and Mittemeijer E 2008 *Acta Mater.* **56** 659–74
- [5] Hosono H, Kim J, Toda Y, Kamiya T and Watanabe S 2017 *PNAS* **114** 233–8
- [6] Nomura K, Takagi A, Kamiya T, Ohta H, Hirano M and Hosono H 2006 *Japan. J. Appl. Phys.* **45** 4303–8
- [7] Park J S, Maeng W J, Kim H S and Park J S 2012 *Thin Solid Films* **520** 1679–93
- [8] Medvedeva J E, Buchholz D B and Chang R P H 2017 *Adv. Electron. Mater.* **3** 1700082
- [9] Houssa M (ed) 2003 *High k Gate Dielectrics* (London: Taylor and Francis) p 641
- [10] Huff H and Gilmer D (ed) 2005 *High Dielectric Constant Materials* (Berlin: Springer) p 710
- [11] Robertson J and Wallace R M 2015 *Mater. Sci. Eng. R* **88** 1–41
- [12] Dimoulas A, Gusev E, McIntyre P C and Heyns M (ed) 2007 *Advanced Gate Stacks for High-Mobility Semiconductors* (Berlin: Springer) p 383
- [13] Houssa M, Dimoulas A and Molle A (ed) 2016 *2D Materials for Nanoelectronics* (Boca Raton, FL: CRC Press) p 467
- [14] Bohra F, Jiang B and Zuo J M 2007 *Appl. Phys. Lett.* **90** 161917
- [15] Kim H, McIntyre P C and Saraswat K C 2003 *Appl. Phys. Lett.* **82** 106–8
- [16] Bersuker G *et al* 2011 *Solid-State Electron.* **65** 146–50
- [17] Grasser T (ed) 2014 *Bias Temperature Instability for Devices and Circuits* (Berlin: Springer) p 810
- [18] Dingemans G and Kessels W 2012 *J. Vac. Sci. Technol. A* **30** 040802
- [19] Nemeth B, Harvey S P, Li J, Young D L, Upadhyaya A, LaSlavia V, Lee B G, Page M R and Stradins P 2017 *Energy Proc.* **124** 295–301
- [20] Bonilla R, Hoex B, Hamer P and Wilshaw P 2017 *Phys. Status Solidi a* **214** 1700293
- [21] Wilk G D, Wallace R M and Anthony J 2001 *J. Appl. Phys.* **89** 5243–75
- [22] Schlom D G, Guha S and Datta S 2008 *MRS Bull.* **33** 1017–25
- [23] Kittl J A *et al* 2009 *ECS Trans.* **19** 29–40
- [24] Clark R D 2014 *Materials* **7** 2913–44
- [25] Lamparter P and Kniep R 1997 *Physica B* **234** 405–6
- [26] Lee S K, Lee S B, Park S Y, Yi Y S and Ahn C W 2009 *Phys. Rev. Lett.* **103** 095501
- [27] Davis S and Gutiérrez G 2011 *J. Phys.: Condens. Matter* **23** 495401
- [28] Buchholz D B, Ma Q, Alducin D, Ponce A, Jose-Yacamán M, Khanal R, Medvedeva J E and Chang R P 2014 *Chem. Mater.* **26** 5401–11
- [29] Petkov V, Holzhueter G, Tröge U, Gerber T and Himmel B 1998 *J. Non-Cryst. Solids* **231** 17–30
- [30] Lushchik A, Lushchik C, Nagirnyi V, Pazylybek S, Sidletskiy O, Schwartz K, Shablonin E, Shugai A and Vasil’chenko E 2013 *Phys. Status Solidi b* **250** 261–70
- [31] Sterrer M, Diwald O, Knözinger E, Sushko P V and Shluger A L 2002 *J. Phys. Chem. B* **106** 12478–82

- [32] Ramo D M, Shluger A, Gavartin J and Bersuker G 2007 *Phys. Rev. Lett.* **99** 155504
- [33] McKenna K P, Wolf M J, Shluger A L, Lany S and Zunger A 2012 *Phys. Rev. Lett.* **108** 116403
- [34] Sezen H *et al* 2015 *Nat. Commun.* **6** 6901
- [35] Wolf M J, McKenna K P and Shluger A L 2012 *J. Phys. Chem. C* **116** 25888–97
- [36] van Dijken A, Meulenkamp E A, Vanmaekelbergh D and Meijerink A 2000 *J. Phys. Chem. B* **104** 1715–23
- [37] Cerbu F *et al* 2016 *Appl. Phys. Lett.* **108** 222901
- [38] Kaviani M, Strand J, Afanas'ev V V and Shluger A L 2016 *Phys. Rev. B* **94** 020103
- [39] Afanas'ev V V, Wang W C, Cerbu F, Madia O, Houssa M and Stesmans A 2014 *ECS Trans.* **64** 17–22
- [40] Wang W C, Badylevich M, Afanas'ev V, Stesmans A, Adelman C, Van Elshocht S, Kittl J, Lukosius M, Walczyk B and Wenger C 2009 *Appl. Phys. Lett.* **95** 132903
- [41] Zahid M B, Aguado D R, Degraeve R, Wang W C, Govoreanu B, Toledano-Luque M, Afanas'ev V and Van Houdt J 2010 *IEEE Trans. Electron Devices* **57** 2907–16
- [42] Wimmer Y, El-Sayed A M, Gös W, Grasser T and Shluger A L 2016 Role of hydrogen in volatile behaviour of defects in SiO₂-based electronic devices *Proc. R. Soc. A* **472** 20160009
- [43] Afanas'ev V V and Adamchuk V K 1994 *Prog. Surf. Sci.* **47** 301–94
- [44] Ma T P and Dressendorfer P V 1989 *Ionizing Radiation Effects in MOS Devices and Circuits* (New York: Wiley) p 608
- [45] Afanas'ev V and Stesmans A 2001 *Europhys. Lett.* **53** 233
- [46] Hartstein A and Young D R 1981 *Appl. Phys. Lett.* **38** 631–3
- [47] El-Sayed A M, Watkins M B, Afanas'ev V V and Shluger A L 2014 *Phys. Rev. B* **89** 125201
- [48] Ando T 2012 *Materials* **5** 478–500
- [49] Ioannou D P 2014 *Microelectron. Reliab.* **54** 1489–99
- [50] Zahid M, Degraeve R, Breuil L, Blomme P, Lisoni J, Van den Bosch G, Van Houdt J and Tang B 2014 Defects characterization of hybrid oating gate/inter-gate dielectric interface in flash memory *IEEE Int. Reliability Physics Symp. (IEEE)* pp 2E–3
- [51] Wang W C, Badylevich M, Adelman C, Swerts J, Kittl J A and Afanas'ev V V 2012 *IOP Conf. Ser.: Mater. Sci. Eng.* **41** 012008
- [52] Afanas'ev V and Stesmans A 2004 *J. Appl. Phys.* **95** 2518–26
- [53] Kerber A and Cartier E A 2009 *IEEE Trans. Device Mater. Reliab.* **9** 147–62
- [54] Cartier E *et al* 2011 *Electron Devices Meeting*
- [55] Molas G *et al* 2009 *Microelectron. Eng.* **86** 1796–803
- [56] Breuil L, Lisoni J G, Blomme P, Van den Bosch G and Van Houdt J 2014 *IEEE Electron Device Lett.* **35** 45–7
- [57] Hoppe E and Aita C 2008 *Appl. Phys. Lett.* **92** 141912
- [58] Strand J, Kaviani M, Afanas'ev V V, Lisoni J G and Shluger A L 2018 *Nanotechnology* **29** 125703
- [59] Afanas'ev V and Stesmans A 2007 *J. Appl. Phys.* **102** 081301
- [60] Afanas'ev V, Stesmans A and Tsai W 2003 *Appl. Phys. Lett.* **82** 245–7
- [61] Gavartin J L, Sushko P V and Shluger A L 2003 *Phys. Rev. B* **67** 035108
- [62] Hausmann D M and Gordon R G 2003 *J. Cryst. Growth* **249** 251–61
- [63] Millon E 2013 *Appl. Surf. Sci.* **278** 2–6
- [64] Gavartin J L and Shluger A L 2007 *Microelectron. Eng.* **84** 2412–15
- [65] Broqvist P, Alkauskas A and Pasquarello A 2008 *Appl. Phys. Lett.* **92** 132911
- [66] Broqvist P, Alkauskas A, Godet J and Pasquarello A 2009 *J. Appl. Phys.* **105** 061603
- [67] Chagarov E A, Porter L and Kummel A C 2016 *J. Chem. Phys.* **144** 084704
- [68] Drabold D 2009 *Eur. Phys. J. B* **68** 1–21
- [69] Greaves G N and Sen S 2007 *Adv. Phys.* **56** 1–116
- [70] Angell C A 1995 *Science* **267** 1924–35
- [71] Ediger M D, Angell C A and Nagel S R 1996 *J. Phys. Chem.* **100** 13200–12
- [72] Debenedetti P G and Stillinger F H 2001 *Nature* **410** 259–67
- [73] Chandler D and Garrahan J P 2010 *Annu. Rev. Phys. Chem.* **61** 191–217
- [74] Kohara S *et al* 2014 *Nat. Commun.* **5** 5892
- [75] Gallington L C *et al* 2017 *Materials* **10** 1290
- [76] Alderman O L G, Skinner L B, Benmore C J, Tamalonis A and Weber J K R 2014 *Phys. Rev. B* **90** 094204
- [77] Skinner L B *et al* 2013 *Phys. Rev. B* **87** 024201
- [78] Johlin E, Wagner L K, Buonassisi T and Grossman J C 2013 *Phys. Rev. Lett.* **110** 146805
- [79] Shluger A L and Stoneham A M 1993 *J. Phys.: Condens. Matter* **5** 3049–86
- [80] Mott N 1987 *J. Phys. C: Solid State Phys.* **20** 3075
- [81] Broglia G, Ori G, Larcher L and Montorsi M 2014 *Modelling Simul. Mater. Sci. Eng.* **22** 065006
- [82] Skinner L B, Benmore C J, Weber K R, Du J, Neuefeind J, Tumber S K and Parise J B 2014 *Phys. Rev. Lett.* **112** 157801
- [83] VandeVondele J, Krack M, Mohamed F, Parrinello M, Chassaing T and Hutter J 2005 *Comput. Phys. Commun.* **167** 103–28
- [84] Guidon M, Hutter J and VandeVondele J 2009 *J. Chem. Theory Comput.* **5** 3010–21
- [85] Lippert G, Hutter J and Parrinello M 1997 *Mol. Phys.* **92** 477–88
- [86] VandeVondele J and Hutter J 2007 *J. Chem. Phys.* **127** 114105
- [87] Goedecker S, Teter M and Hutter J 1996 *Phys. Rev. B* **54** 1703–10
- [88] Lany S and Zunger A 2009 *Modelling Simul. Mater. Sci. Eng.* **17** 084002
- [89] Lany S and Zunger A 2008 *Phys. Rev. B* **78** 235104
- [90] Iannuzzi M, Chassaing T, Wallman T and Hutter J 2005 *CHIMIA Int. J. Chem.* **59** 499–503
- [91] Heifets E N and Shluger A L 1992 *J. Phys.: Condens. Matter* **4** 8311–20
- [92] Varley J B, Janotti A, Franchini C and de Walle C G V 2012 *Phys. Rev. B* **85** 081109
- [93] Cohen A J, Mori-Sanchez P and Yang W 2012 *Chem. Rev.* **112** 289–320
- [94] Vosko S H and Wilk L 1983 *J. Phys. B: At. Mol. Phys.* **16** 3687–702
- [95] Lundberg M and Siegbahn P E M 2005 *J. Chem. Phys.* **122** 224103
- [96] Lægsgaard J and Stokbro K 2001 *Phys. Rev. Lett.* **86** 2834–7
- [97] Pacchioni G, Frigoli F, Ricci D and Weil J A 2001 *Phys. Rev. B* **63** 054102
- [98] Mardirossian N and Head-Gordon M 2017 *Mol. Phys.* **115** 2315–72
- [99] Wang Z, Brock C, Matt A and Bevan K H 2017 *Phys. Rev. B* **96** 125150
- [100] Lany S and Zunger A 2009 *Phys. Rev. B* **80** 085202
- [101] Erhart P, Klein A, Åberg D and Sadigh B 2014 *Phys. Rev. B* **90** 035204
- [102] Atalla V, Zhang I Y, Hofmann O T, Ren X, Rinke P and Scheffler M 2016 *Phys. Rev. B* **94** 035140
- [103] Perdew J P, Parr R G, Levy M and Balduz J J L 1982 *Phys. Rev. Lett.* **49** 1691–4
- [104] Huang S, Verma P and Truhlar D G 2017 *J. Phys. Chem. C* **121** 23955–63
- [105] Heyd J, Scuseria G E and Ernzerhof M 2003 *J. Chem. Phys.* **118** 8207–15
- [106] Krukau A V, Vydrov O A, Izmaylov A F and Scuseria G E 2006 *J. Chem. Phys.* **125** 224106
- [107] Dicks O and Shluger A 2017 *J. Phys.: Condens. Matter* **29** 314005
- [108] Bell R and Dean P 1970 *Discuss. Faraday Soc.* **50** 55–61

- [109] Chang T M, Bauer J and Skinner J 1990 *J. Chem. Phys.* **93** 8973–82
- [110] Dong J and Drabold D 1996 *Phys. Rev. B* **54** 10284
- [111] Drabold D A, Stephan U, Dong J and Nakhmanson S M 1999 *J. Mol. Graph. Modelling* **17** 285–91
- [112] Unge M and Christen T 2014 *Chem. Phys. Lett.* **613** 15–8
- [113] Youn Y, Kang Y and Han S 2014 *Comput. Mater. Sci.* **95** 256–62
- [114] Anderson P 1972 *Proc. Natl Acad. Sci. USA* **69** 1097–9
- [115] Gavartin J L and Shluger A L 2001 *Phys. Rev. B* **64** 245111
- [116] Kaviani M, Koleini M and Shluger A L 2018 unpublished
- [117] Garvie L A, Alvarez J R, Rez P, Buseck P R, Craven A J and Brydson R 2000 *Am. Mineral.* **85** 732–38
- [118] El-Sayed A M, Tanimura K and Shluger A L 2015 *J. Phys.: Condens. Matter* **27** 265501
- [119] Gao D Z, El-Sayed A M and Shluger A L 2016 *Nanotechnology* **27** 505207
- [120] Guo Z, Ambrosio F and Pasquarello A 2016 *Appl. Phys. Lett.* **109** 062903
- [121] Dicks O, Cottom J, Afanas'ev V V and Shluger A L *Phys. Rev. Appl.* submitted
- [122] Landmann M, Köhler T, Köppen S, Rauls E, Frauenheim T and Schmidt W 2012 *Phys. Rev. B* **86** 064201
- [123] Köhler T, Turowski M, Ehlers H, Landmann M, Ristau D and Frauenheim T 2013 *J. Phys. D: Appl. Phys.* **46** 325302
- [124] Yang S, Brant A T, Giles N C and Halliburton L E 2013 *Phys. Rev. B* **87** 125201
- [125] Yim C M, Watkins M B, Wolf M J, Pang C L, Hermansson K and Thornton G 2016 *Phys. Rev. Lett.* **117** 116402
- [126] Eagles D 1964 *J. Phys. Chem. Solids* **25** 1243–51
- [127] Macdonald I R, Howe R F, Zhang X and Zhou W 2010 *J. Photochem. Photobiol. A* **216** 238–43
- [128] Chiesa M, Paganini M C, Livraghi S and Giamello E 2013 *Phys. Chem. Chem. Phys.* **15** 9435–47
- [129] Sezen H, Buchholz M, Nefedov A, Natzeck C, Heissler S, Di Valentin C and Wöll C 2014 *Sci. Rep.* **4** 3808
- [130] Deák P, Aradi B and Frauenheim T 2011 *Phys. Rev. B* **83** 155207
- [131] Deák P, Aradi B and Frauenheim T 2012 *Phys. Rev. B* **86** 195206
- [132] Zawadzki P, Jacobsen K W and Rossmeisl J 2011 *Chem. Phys. Lett.* **506** 42–5
- [133] Janotti A, Franchini C, Varley J, Kresse G and Van de Walle C 2013 *Phys. Status Solidi* **7** 199–203
- [134] Tabriz M F, Aradi B, Frauenheim T and Deák P 2017 *J. Phys.: Condens. Matter* **29** 394001
- [135] Spreafico C and VandeVondele J 2014 *Phys. Chem. Chem. Phys.* **16** 26144–52
- [136] Selçuk S and Selloni A 2017 *J. Phys. D: Appl. Phys.* **50** 273002
- [137] Tang H, Berger H, Schmid P, Levy F and Burri G 1993 *Solid State Commun.* **87** 847–50
- [138] Setvín M, Franchini C, Hao X, Schmid M, Janotti A, Kaltak M, Van de Walle C G, Kresse G and Diebold U 2014 *Phys. Rev. Lett.* **113** 086402
- [139] Deskins N A, Du J and Rao P 2017 *Phys. Chem. Chem. Phys.* **19** 18671–84
- [140] Erhart P, Albe K and Klein A 2006 *Phys. Rev. B* **73** 205203
- [141] Sabino F P, Besse R, Oliveira L N, Wei S H and Da Silva J L 2015 *Phys. Rev. B* **92** 205308
- [142] Nahm H H and Kim Y S 2014 *NPG Asia Mater.* **6** e143
- [143] Hosono H 2006 *J. Non-Cryst. Solids* **352** 851–8
- [144] Schirmer O F 2006 *J. Phys.: Condens. Matter* **18** R667–704
- [145] Schirmer O F 2011 *J. Phys.: Condens. Matter* **23** 334218
- [146] Maglionone M 2016 *J. Adv. Dielectr.* **6** 1630006
- [147] Griscom D L 2006 *J. Non-Cryst. Solids* **352** 2601–17
- [148] Kimmel A V, Sushko P V and Shluger A L 2007 *J. Non-Cryst. Solids* **353** 599–604
- [149] Camellone M F, Khne T D and Passerone D 2009 *Phys. Rev. B* **80** 033203
- [150] Strand J, Dicks O A, Kaviani M and Shluger A L 2017 *Microelectron. Eng.* **178** 235–9
- [151] Chen S and Wang L W 2014 *Phys. Rev. B* **89** 014109
- [152] McPherson J W 2012 *Microelectron. Reliab.* **52** 1753–60
- [153] Padovani A, Gao D Z, Shluger A L and Larcher L 2017 *J. Appl. Phys.* **121** 155101
- [154] Foster A S, Gejo F L, Shluger A L and Nieminen R M 2002 *Phys. Rev. B* **65** 174117
- [155] Traoré B, Blaise P, Vianello E, Jalaguier E, Molas G, Nodin J, Perniola L, Salvo B D and Nishi Y 2014 *IEEE Int. Reliability Physics Symp.* pp 5E2.1–2.5
- [156] Bradley S R, Shluger A L and Bersuker G 2015 *Phys. Rev. Appl.* **4** 064008
- [157] Ramo D M, Gavartin J, Shluger A and Bersuker G 2007 *Phys. Rev. B* **75** 205336
- [158] Traoré B, Blaise P and Sklénard B 2016 *J. Phys. Chem. C* **120** 25023–9
- [159] Strand J, Kaviani M and Shluger A L 2017 *Microelectron. Eng.* **178** 279–83
- [160] Gao D Z, Strand J, El-Sayed A M, Shluger A, Padovani A and Larcher L 2018 *IEEE-IRPS Proc.* submitted
- [161] Kimmel A, Sushko P, Shluger A and Bersuker G 2009 *ECS Trans.* **19** 3–17
- [162] Vandelli L, Padovani A, Larcher L, Southwick R G, Knowlton W B and Bersuker G 2011 *IEEE Trans. Electron Devices* **58** 2878–87
- [163] Abdellouahed S and McKenna K P 2015 *J. Appl. Phys.* **118** 134103
- [164] Park M H *et al* 2015 *Adv. Mater.* **27** 1811–31
- [165] Böschke T, Müller J, Bräuhaus D, Schröder U and Böttger U 2011 *Appl. Phys. Lett.* **99** 102903
- [166] Polakowski P and Müller J 2015 *Appl. Phys. Lett.* **106** 232905
- [167] Müller J, Polakowski P, Müller S and Mikolajick T 2015 *ECS J. Solid State Sci. Technol.* **4** N30–5
- [168] Karda K, Jain A, Mouli C and Alam M A 2015 *Appl. Phys. Lett.* **106** 163501
- [169] Govoreanu B, Degraeve R, Zahid M, Nyns L, Cho M, Kaczer B, Jurczak M, Kittl J and Van Houdt J 2009 *Microelectron. Eng.* **86** 1807–11
- [170] Kuhnhold-Pospischil S, Saint-Cast P, Hofmann M, Weber S, Jakes P, Eichel R A and Granwehr J 2016 *J. Appl. Phys.* **120** 195304
- [171] Kuhnhold-Pospischil S, Saint-Cast P, Richter A and Hofmann M 2016 *Appl. Phys. Lett.* **109** 061602
- [172] Govoreanu B *et al* 2016 *Proc. 36th IEEE Symp. on VLSI Technology (Honolulu, HI, USA)* pp 82–83
- [173] Clima S, Chen Y Y, Fantini A, Goux L, Degraeve R, Govoreanu B, Pourtois G and Jurczak M 2015 *IEEE Electron Device Lett.* **36** 769–71
- [174] Belmonte A, Govoreanu B, Subhechha S, Piazza L D, Goux L and Kar G S 2017 *IEEE Int. Reliability Physics Symp. (Monterey, CA, USA)* pp PM10.1–10.5
- [175] Afanas'ev V, Kolomiets N, Houssa M and Stesmans A 2018 *Phys. Status Solidi a* **215** 1700865
- [176] Joly J F, Béland L K, Brommer P and Mousseau N 2013 *Phys. Rev. B* **87** 144204
- [177] Béland L K, Osetsky Y N, Stoller R E and Xu H 2015 *Comput. Mater. Sci.* **100** 124–34
- [178] Ceresoli D and Vanderbilt D 2006 *Phys. Rev. B* **74** 125108
- [179] Mott N F and Davis E A 1979 *Electronic Processes in Non-Crystalline Materials* (Oxford: Clarendon)
- [180] Tessler N, Preezant Y, Rappaport N and Roichman Y 2009 *Adv. Mater.* **21** 2741–61
- [181] Dimitrijevic N M, Saponjic Z V, Rabatic B M, Poluektov O G and Rajh T 2007 *J. Phys. Chem. C* **111** 14597–601